Metrologia



# Two-capillary viscometer for temperatures and pressures relevant to $CO_2$ capture, transport, and storage—operation and improved analysis at high pressure

OPEN ACCESS
IOP Publishing | Bureau International des Poids et Mesures Metrologia
Metrologia **61** (2024) 035009 (24pp) https://doi.org/10.1088/1681-7575/ad435e

# Two-capillary viscometer for temperatures and pressures relevant to $CO_2$ capture, transport, and storage—operation and improved analysis at high pressure

**Bahareh Khosravi[1,*], Anders Austegard[2], Sigurd W Løvseth[2], H G Jacob Stang[2] and Jana P Jakobsen[1]**

[1] Norwegian University of Science and Technology, Trondheim, Norway
[2] SINTEF Energy Research, Trondheim, Norway

E-mail: bahareh.khosravi@ntnu.no

Received 3 June 2023, revised 23 April 2024
Accepted for publication 25 April 2024
Published 22 May 2024

**Abstract**

High-pressure viscosity measurements are crucial for understanding $CO_2$ transport and storage because $CO_2$ is often transported as a supercritical fluid, at a high pressure and temperature above its critical point. In this study, we extended the operational range of our new two-capillary viscometer to handle pressures up to 20 MPa, focusing on the behaviour of $CO_2$ at temperatures around 300 K. The analysis model is based on the low-pressure principle, which relied on virial descriptions of density and viscosity, proved inadequate under these conditions. Therefore, we introduced a modified hydrodynamic model as a function of density that is suitable for viscosity measurements at high pressure and liquid states. The modified model bypasses the need for a density virial correction. We conducted initial viscosity tests on pure $CO_2$ at five isotherms: 280.01 K, 298.15 K, 300.01 K, 323.15 K, and 348.15 K to validate the performance of the new two capillary viscometer and the modified model at high pressures. The experimental viscosities agreed with the model predictions and comparable within the estimated uncertainty of the data. In addition, we thoroughly explained the calibrations and the analysis of uncertainty estimation. The uncertainty analysis showed a maximum extended combined uncertainty of 1.3% ($k = 2$) within all thermodynamic states—gas, liquid, and close to the critical region.

Keywords: viscosity, CO2, two-capillary viscometer, high-pressure measurements

* Author to whom any correspondence should be addressed.



 

## 1. Introduction

Carbon capture and storage (CCS) is a crucial technology for mitigating greenhouse gas emissions and combating climate change. One of the key challenges in CCS is managing impurities in the CO2 stream after capture [1]. Impurities can have a significant impact on the design and operation of CCS processes, as well as on the safety and long-term stability of the storage sites. To address these challenges, a range of technologies and strategies have been developed for managing impurities in CCS systems. However, understanding the role of impurities in CO2 stream behaviour and possible interactions with applied materials or the storage environment is still critical for developing safe and effective systems for CCS. Viscosity is particularly important in the context of CO2 transport and storage because CO2 is often transported as a supercritical fluid, at a high pressure and temperature above its critical point. Under these conditions, the viscosity of CO2 can be significantly affected by impurities often present in the CO2 captured from the industrial processes. Higher viscosity can increase the pressure drop in pipelines, reduce the flow rate of CO2, and increase the energy requirements for pumping and compressing CO2. Additionally, high viscosity can lead to the accumulation of deposits or scaling on the walls of pipelines and equipment, which can increase the risk of corrosion and mechanical damage. Understanding the effect of impurities on the viscosity of CO2 is critical for design and safe operation of efficient CCS systems [2]. Therefore, accurate measurement and modelling of the viscosity of CO2 with different impurities at relevant pressures and temperatures are required. Improved understanding and extended database will enable to optimize the design and operation of CO2 transport and storage systems and minimize their environmental and economic impact.

Measuring viscosity to an acceptable accuracy is difficult because it requires sophisticated equipment and a complete working theory. Several extensive reviews of available experimental data and models for the transport properties of CO2-mixtures relevant to CO2 capture, transport, and storage have been published [3–5]. These reviews show that the data available for CO2 viscosity in the presence of impurities in the liquid and supercritical regions are very limited. One data set published the viscosity data for pure CO2 and five binary CO2-impurity mixtures in the liquid and the supercritical region which is limited to one composition of mixture [6]. The second reference measured the viscosity of three multi-component CO2-rich mixtures at pressures from 1 MPa to 155 MPa and various temperatures from 243 K to 423 K in the gas, liquid, and supercritical regions [7]. In a recent work, the viscosity data for CO2 with impurities N2 and H2 are published, but no data in the liquid phase were reported [8, 9]. Data for binary mixtures of $CO_2$ and any of the many components commonly occurring in $CO_2$ streams such as $H_2S$, COS, NO, $NO_2$, $N_2O_4$, $NH_3$, amines, and $H_2O$ have not been reported yet. Data are still limited also regarding the gas phase of $CO_2$-rich mixtures.

To address the lack of viscosity data for CO2-rich mixtures, a new two-capillary viscometer was constructed. The details of the apparatus design and construction can be found in our previous work [10]. This new two-capillary viscometer was built based on the principles of measuring the viscosity ratio when one capillary works as a viscometer and one capillary as a flow meter [11]. In this work, a different approach than what Berg *et al* [12] proposed was implemented to use the two-capillary viscometer for both high-pressure and liquids phases measurements. In this paper, the new approach and the modified hydrodynamic model are introduced, which are applicable for $CO_2$ and $CO_2$ rich mixtures. The performance of the two-capillary viscometer and the modified model was validated for pure $CO_2$ in gas phase, liquid phase and close to the critical region. Measured viscosity was compared with existing experimental data and data calculated using the reference viscosity correlation [13] implemented in the NIST REFPROP 10.0 database [14].

This manuscript is organized as follows: section 2 describes the experimental methodology; section 3 outlines the measurement principles; experimental section is explained in section 4; and section 5 presents the results and discussion for the viscosity of pure $CO_2$ obtained from the new two-capillary viscometer, the uncertainty estimation, and the comparison of the obtained results with the results available in the literature, following by conclusion.

## 2. Experimental methodology

### 2.1. The theory of capillary viscometers: incompressible fluids

The principle of capillary viscometers is based on the Hagen–Poiseuille equation [15] as viscosity and flow rate are inversely related. For an incompressible fluid flowing through a capillary tube with a radius of $r$ and length $L$, the relation between the pressure drop along the capillary and the volumetric flow rate of $\dot{Q}$ can be described as:

$$\dot{Q} = \frac{\pi r^4 (P_{\text{in}} - P_{\text{out}})}{8 \eta L} \tag{1}$$

where $\eta$ is the viscosity of the fluid and, $P$in and $P$out are the pressures at the inlet and outlet of the capillary. The assumptions for the basic Hagen–Poiseuille equation to be valid are: (i) the fluid is incompressible, (ii) the fluid is Newtonian, (iii) the flow regime is laminar and steady, (iv) the ratio of the inner diameter $r$ to the length $L$ is small, (v) the cross section along the capillary is constant and uniform, (vi) the capillary is straight, (vii) the temperature is constant and temperature changes due to expansion or viscous dissipation are negligible, and (viii) the capillary wall slip effect is insignificant [16].

### 2.2. Fluid dynamic model for gases at low pressure: a single capillary viscometer for absolute measurement

The Hagen–Poiseuille equation [15] can be used for a volumetric gas flow if the compressibility of the fluid is considered. Gas compressibility reduces the volumetric gas flow in the viscometer. The volumetric flow rate can be obtained using the

ratio between the molar flow rate $\dot{n}$ or the mass flow rate $\rho$ and the density $\rho$ of the fluid as:

$$\dot{Q} = \frac{M\dot{n}}{\rho} = \frac{\dot{m}}{\rho} \tag{2}$$

where $M$ is the molar mass of the fluid. A differential equation can be formulated by combining the two expressions for volumetric flow rate (1) and (2) at location $z$ with temperature $T$ and pressure $P$. Integrated along the whole capillary length $L$ it can be written as [16]:

$$\int_{P_{\text{in}}}^{P_{\text{out}}} \frac{\rho(T,P)}{\eta(T,P)} \mathrm{d}P = \int_{0}^{L} -\frac{8M\dot{n}}{\pi r^4} \mathrm{d}z. \tag{3}$$

Equation (3) can be used for a compressible fluid. The molar flow rate using ideal gas assumption after the integration over the pressure of $P$ yields:

$$\dot{n}_0 = \frac{\pi r^4 \left(P_{\text{in}}^2 - P_{\text{out}}^2\right)}{16L\eta^{\text{gas}}(T,0)\, R_{\text{gas}} T} \tag{4}$$

where $R_{\text{gas}}$ is the universal gas constant and $\eta^{\text{gas}}(T,0)$ is the viscosity of an ideal gas at the limit of zero-pressure. To compensate for the assumptions (i)–(viii) described for the basic Hagen–Poiseuille equation (1), Berg [16] implemented several correction terms. Based on these correction terms, a more accurate hydrodynamic model for compressible fluids flowing through a capillary winding into a coil with a radius of *R*curve will have the form of:

$$\begin{aligned}\dot{n} &= \dot{n}_0 \left[1 + g_{\text{virial}}(P_{\text{in}}, P_{\text{out}}) + 4K_{\text{slip}}Kn + \frac{K_{\text{ent}}}{16}\frac{r}{L}Re \right. \\ &\left. + \left(\frac{K_{\text{exp}}}{8} + \frac{K_{\text{thermal}}}{16}\right)\frac{r}{L}Re \ln\left(\frac{P_{\text{out}}}{P_{\text{in}}}\right)\right] f_{\text{cent}}(De,\delta) \\ &= \dot{n}_0 \left(1 + \sum_{i=1}^{5} c_i\right) f_{\text{cent}}(De,\delta) = \dot{n}_0\, \mathrm{C}^{\text{gas}}(T, P_{\text{in}}, P_{\text{out}})\end{aligned} \tag{5}$$

where *Kn, Re, De*, and $\delta$ are the Knudsen number, the Reynolds number, the Dean number and the ratio of the internal radius $r$ of the capillary to the radius of coil, *R*curve, respectively. These dimensionless parameters are defined as follows:

$$Kn \equiv \frac{1}{r}\left(\frac{2R_{\text{gas}}T}{M}\right)^{\frac{1}{2}} \left(\frac{\eta\left(T, P_{1/2}\right)}{P_{1/2}}\right) \tag{6}$$

$$Re \equiv \frac{2M\dot{n}}{\pi r \eta(T, \bar{P}_{\text{in,out}})} \tag{7}$$

$$De \equiv Re \times (\delta)^{\frac{1}{2}} \tag{8}$$

$$\delta = \frac{r}{R_{\text{curve}}} \tag{9}$$

where the average pressure along the capillary is assumed to be that of an ideal gas:

$$\bar{P}_{\text{in,out}} = \frac{2}{3}\left(\frac{{P_{\text{in}}}^3 - {P_{\text{out}}}^3}{{P_{\text{in}}}^2 - {P_{\text{out}}}^2}\right). \tag{10}$$

The molar flow $\dot{n}$ is proportional to three factors, namely: (1) the flow rate for an ideal gas ($\dot{n}_0$) computed from equation (4), (2) the correction for centrifugal effect ($f_{\text{cent}}$) due to curving the capillary into a coil, and (3) five dimensionless correction terms. The dimensionless correction terms are: (A) deviations from the ideal gas behaviour; $g_{\text{virial}}$, (B) slip at the capillary walls; $K_{\text{slip}}$, (C) kinetic energy changes at the capillary entrance; $K_{\text{ent}}$, (D) gas expansion along the length of the capillary which increases the kinetic energy, causing additional pressure drop; $K_{\text{exp}}$, and (E) thermal or radial temperature distribution along the capillary; $K_{\text{thermal}}$. A more detailed description of the correction terms (A)–(E) and the model proposed for $f_{\text{cent}}$ can be found in the work by Berg [16].

The working equation (4) shows that accurate data on capillary geometry ($r$ and $L$), fluid flow rate, and pressure at the inlet and outlet of the capillary are the main parameters needed for the viscosity calculation.

*2.2.1. Virial correction factors for gases.* To correct for the effect on flow rate, caused by deviation from ideal gas behaviour, correction factors need to be introduced for the density and viscosity. With reference to equation (3), for a non-ideal gas for the capillary with the length of $L$:

$$\int_{P_{\text{in}}}^{P_{\text{out}}} \frac{\rho(T,P)}{\eta(T,P)} \mathrm{d}P = -\frac{8M\dot{n}L}{\pi r^4}. \tag{11}$$

Berg [16] used the virial equation of state to predict the behaviour of a non-ideal gas. For density, the virial expansion was written and by keeping only the second order terms:

$$\rho \approx \frac{M}{R_{\text{gas}}T}\frac{P}{1 + B_\rho P + C_\rho P^2} \tag{12}$$

where $B_\rho$ and $C_\rho$ are the second and third pressure virial coefficients for density, respectively. For viscosity, virial expansion to second order gives:

$$\eta(T,P) \approx \eta(T,0)\left[1 + b_\eta P + (c_\eta - b_\eta B_\rho) P^2\right] \tag{13}$$

where $b_\eta$ and $(c_\eta - b_\eta B_\rho)$ are the second and third virial coefficients when the viscosity is described as a function of pressure. By combing the virial viscosity and density coefficients, the molar flow rate after integration gives:

$$\dot{n} \approx \dot{n}_0 \left[1 + g_{\text{virial}}(P_{\text{in}}, P_{\text{out}})\right] \tag{14}$$

$$\begin{aligned} g_{\text{virial}}(P_{\text{in}}, P_{\text{out}}) \cong &-(B_\rho + b_\eta)\bar{P} \\ &- \left[C_\rho + c_\eta - (B_\rho + b_\eta)^2\right]\frac{\left(P_{\text{in}}^2 + P_{\text{out}}^2\right)}{2}. \end{aligned} \tag{15}$$

The virial parameters can be found from models or when possible, from simple correlations of the measurement data in an iterative manner.

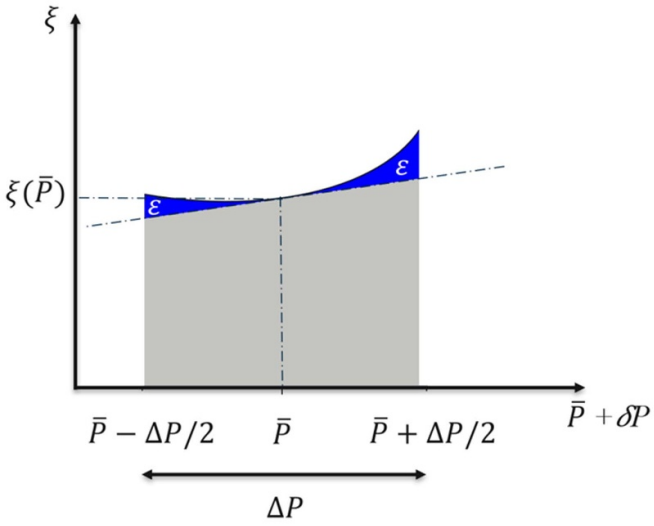


**Figure 1.** The ratio of inverse kinematic viscosity, $\boldsymbol{\xi}$ $(\boldsymbol{P})$, over pressure drop along the capillary.

### *2.3. Fluid dynamic model for gases at high pressure or liquid phase: a single capillary viscometer for absolute measurement*

In this work, the model by Berg [16] was modified for liquids and fluids in a dense phase. Equation (4) manifests itself after integration of equation (3) with respect to the ideal gas law. For a nearly ideal gas, the integral, equation (3), can be calculated relatively accurately since the pressure dependence of the viscosity is small and the density dependence is known. However, the corrected flow rate in equation (5) is not applicable for liquid phase. Under non-ideal conditions, the density and viscosity change along the capillary along with the pressure. Changes in pressure and viscosity must be considered. The density/viscosity ratio in equation (3) is the invers kinematic viscosity and is defined for a given temperature as:

$$\xi\,(P) = \frac{\rho\,(P)}{\eta\,(P)}. \tag{16}$$

Considering a polynomial expression for $\xi$ as a function of the pressure drop $\delta P$, as illustrated in figure 1. The local pressure $P$ can be written as the deviation $\delta P$ from the average pressure $\bar{P}$, so that equation (16) becomes:

$$\begin{aligned}\xi\,(\delta P) = \xi\,(\bar{P}+\delta P) = \xi_0 + \xi_1\,(\delta P) + \xi_2(\delta P)^2 \\ + \xi_3(\delta P)^3 + \ldots\end{aligned} \tag{17}$$

Function $\xi$ can be represented as a Taylor series for the average pressure $\bar{P}_{\mathrm{in,out}}$ at any location in the capillary with the pressure $P$:

$$\begin{aligned}\delta P &= P - \bar{P}_{\mathrm{in,out}} \\ \Delta P &= P_{\mathrm{in}} - P_{\mathrm{out}}\end{aligned} \tag{18}$$

$$\xi_0 = \xi\,(\bar{P}_{\mathrm{in,out}}), \xi_1 = \frac{\partial \xi\,(\bar{P}_{\mathrm{in,out}})}{\partial P}, \xi_2 = \frac{1}{2}\frac{\partial \xi^2\,(\bar{P}_{\mathrm{in,out}})}{\partial P^2}. \tag{19}$$

Consequently,

$$\begin{aligned}\int_{P_{\mathrm{out}}}^{P_{\mathrm{in}}} \xi\,(P)\,dP &= \int_{\bar{P}_{\mathrm{in,out}}-\Delta P/2}^{\bar{P}_{\mathrm{in,out}}+\Delta P/2} \xi\,(P)\,dP = \int_{-\Delta P/2}^{\Delta P/2} \xi\,(\delta P)\,d(\delta P) \\ &= \int_{-\Delta P/2}^{\Delta P/2} \left(\xi_0 + \xi_1\delta P + \xi_2\delta P^2 + \xi_3\delta P^3 + \cdots\right) d(\delta P). \\ &= \left[\xi_0\delta P + \frac{\xi_1}{2}\delta P^2 + \frac{\xi_2}{3}\delta P^3 + \frac{\xi_3}{4}\delta P^4 + \cdots\right]_{-\Delta P/2}^{\Delta P/2} \\ &\approx \xi_0\Delta P + \frac{\xi_2}{12}\Delta P^3\end{aligned} \tag{20}$$

Inserting the relationship in equation (19) into equation (20) yields:

$$\int_{P_{\mathrm{out}}}^{P_{\mathrm{in}}} \xi\,(P)\,\mathrm{d}P \cong \Delta P\xi\,(\bar{P}_{\mathrm{in,out}}) \left(1 + \frac{\Delta P^2}{24\xi\,(\bar{P}_{\mathrm{in,out}})}\frac{\partial^2\xi\,(\bar{P}_{\mathrm{in,out}})}{\partial P^2}\right). \tag{21}$$

For a linear approximation of the function $\xi$, the neglected quadratic term causes a relative error of

$$\varepsilon\,(\bar{P}_{\mathrm{in,out}}) = \frac{1}{24}\frac{\frac{\partial^2\xi\,(\bar{P}_{\mathrm{in,out}})}{\partial P^2}}{\xi\,(\bar{P}_{\mathrm{in,out}})} \tag{22}$$

$$\int_{P_{\mathrm{out}}}^{P_{\mathrm{in}}} \xi\,(P)\,\mathrm{d}P \approx \Delta P\xi\,(\bar{P}_{\mathrm{in,out}})\left(1 + \varepsilon\,(\bar{P}_{\mathrm{in,out}})\,\Delta P^2\right). \tag{23}$$

Therefore, if it is proven that the error term $\varepsilon\,(\bar{P}_{\mathrm{in,out}})\,\Delta P^2$ is small (within the uncertainty of the measurements), the integral can be approximated with a linear relation. In this work, $\xi\,(\delta P)$ is assumed to be linear since the pressure drop is small. However, for accurate measurements, it is important to estimate the error introduced by this assumption. Section 5.3.2 shows that the error is within the uncertainty of the measurements. Here, we obtain an expression for the molar flow rate by ignoring the small error term $\varepsilon\,(\bar{P}_{\mathrm{in,out}})\,\Delta P^2$

$$\int_{P_{\mathrm{out}}}^{P_{\mathrm{in}}} \xi\,(P)\,\mathrm{d}P \approx \Delta P\xi\,(\bar{P}_{\mathrm{in,out}}) \approx \frac{\rho\,(T,\bar{P}_{\mathrm{in,\,out}})}{\eta\,(T,\bar{P}_{\mathrm{in,out}})}\,(P_{\mathrm{in}} - P_{\mathrm{out}}). \tag{24}$$

Finally, the molar flow rate can be written by using equations (4), (5), (11) and (24):

$$\dot{n}^{\mathrm{fld}} = \frac{\pi r^4\,\rho^{\mathrm{fld}}\,(T,\bar{P}_{\mathrm{in,out}})\,(P_{\mathrm{in}} - P_{\mathrm{out}})}{8\mathrm{M}L\eta^{\mathrm{fld}}\,(T,\bar{P}_{\mathrm{in,out}})}\mathrm{C}'_{\mathrm{Hp}}\,(T,P_{\mathrm{in}},P_{\mathrm{out}}) \tag{25}$$

where the superscript 'fld' denotes the test fluid. The high-pressure correction factor $\mathrm{C}'_{\mathrm{Hp}}$ includes the same correction described for $C$ in equation (5), except the term $g_{\mathrm{virial}}$. The density has already been considered in the main equation and the density virial coefficients in equation (15) become zero.

The $g_{\text{virial}}$ at high pressures does not include the viscosity virial correction due to the use of equation (25). $g_{\text{virial}}$ only needs to be considered at low densities. Hence expression for $C'_{Hp}$ is:

$$C'_{Hp}(T,P_{in},P_{out}) = \left[1+4K_{slip}Kn+\frac{K_{ent}}{16}\frac{r}{L}\text{Re} + \left(\frac{K_{exp}}{8}+\frac{K_{thermal}}{16}\right)\frac{r}{L}\text{Re}\ln\left(\frac{P_{out}}{P_{in}}\right)\right] f_{cent}(De,\delta). \quad (26)$$

Alternatively, for viscosity at zero pressure:

$$\dot{n}^{fld} = \frac{\pi r^4 \rho^{fld}(T,\bar{P}_{in,out})(P_{in}-P_{out})}{8\,ML\eta^{fld}(T,0)} C'_{Lp}(T,P_{in},P_{out}). \quad (27)$$

With $C'_{Lp}$ including the virial correction for the pressure effect of viscosity, which only work for low pressure:

$$g'_{\text{virial, Lp}}(P_{in},P_{out}) \cong -b_\eta \bar{P} - \left[c_\eta - b_\eta{}^2\right] \times \frac{\left(P_{in}^2+P_{out}^2\right)}{2}, \quad (28)$$

$$C'_{Lp} = \left[1+g'_{\text{virial, Lp}}(P_{in},P_{out})+4K_{slip}Kn+\frac{K_{ent}}{16}\frac{r}{L}\text{Re} + \left(\frac{K_{exp}}{8}+\frac{K_{thermal}}{16}\right)\frac{r}{L}\text{Re}\ln\left(\frac{P_{out}}{P_{in}}\right)\right] f_{cent}(De,\delta). \quad (29)$$

### *2.4. Fluid dynamic model for gases at high pressure or liquid phase: a two-capillary viscometer and ratio measurement*

The ratio between two viscosities can be measured more accurately than absolute measurements because the impact of capillary geometry on the uncertainty of the measurements is cancelled out in the ratio equation. The working equation proposed by May *et al* [11] for low densities is:

$$\eta^{fld}_{0,T} = \eta^{He}_{0,T_{ref}} \left(\frac{\eta^{He}_{0,T}}{\eta^{He}_{0,T_{ref}}}\right)_{ab\ initio} \left(\frac{\eta^{fld}_{0,T_{ref}}}{\eta^{He}_{0,T_{ref}}}\right) R^{fld,\,He}_{T,T_{ref}}. \quad (30)$$

The fluid dynamic model used for fluids in dense phases and liquids is similar to viscosity ratio measurements at low densities. However, the effect of high pressures on the capillary needs to be investigated by adding the factor $\left(\eta^{He}_{P,T}/\eta^{He}_{0,T}\right)$ compared to the low-pressure measurements. The working equation proposed by Berg *et al* [12] is:

$$\eta^{fld}_{P,T} = \eta^{He}_{0,T_{ref}} \left(\frac{\eta^{He}_{0,T}}{\eta^{He}_{0,T_{ref}}}\right)_{ab\ initio} \left(\frac{\eta^{fld}_{0,T_{ref}}}{\eta^{He}_{0,T_{ref}}}\right) \left(\frac{\eta^{He}_{P,T}}{\eta^{He}_{0,T}}\right) \left(R^{fld,\,He}_{T,T_{ref}}\right)_{P,0} \quad (31)$$

where:

(1) $\eta^{He}_{0,T_{ref}}$ is the viscosity of helium at zero density and the reference temperature of 298.15 K calculated using *ab initio* [17] from quantum mechanics and statistical mechanics with uncertainty less than 0.01%.

(2) $\left(\eta^{He}_{0,T}/\eta^{He}_{0,T_{ref}}\right)_{abinitio}$ is the temperature-dependent ratio for helium at 298.15 K and desired temperature $T$, calculated *ab initio* [17] with uncertainty less than 0.01% in the range 200 K $< T <$ 400 K.

(3) $\left(\eta^{fld}_{0,T_{ref}}/\eta^{He}_{0,T_{ref}}\right)$ is a reference value for the viscosity ratio, measured at 298.15 K. This ratio can be determined using downstream capillary as a single capillary viscometer once for fluid under test and once for helium. Using the single capillary viscometer demands the flow measurement, explained in section 3.1.

(4) $\left(\eta^{He}_{P,T}/\eta^{He}_{0,T}\right)$ is the pressure-dependent ratio for helium at a desired temperature. This ratio can be determined from helium measurement calibration, and it will be further elaborated in section 3.2.

(5) $\left(R^{fld,\,He}_{T,T_{ref}}\right)_{P,0}$ is the measurement of the temperature-dependent ratio using the two-capillary viscometer and will be further elaborated in section 3.3. The viscosity ratio is defined as:

$$\left(R^{fld,\,He}_{T,T_{ref}}\right)_{P,0} = \left(\frac{\eta^{fld}_{P,T}}{\eta^{fld}_{0,T_{ref}}}\right) \Big/ \left(\frac{\eta^{He}_{P,T}}{\eta^{He}_{0,T_{ref}}}\right). \quad (32)$$

## 3. Principle of the measurements

The two-capillary viscometer was designed in accordance with the principles set out above. A simplified schematic of the two-capillary viscometer is shown in figure 2. A detailed description of the apparatus can be found in our previous work [10].

The new two-capillary viscometer works by setting the upstream capillary to the desired temperature and pressure where the pressure point of measurement refers to an average pressure in the upstream capillary; $P = P_{1,2} = (P_1+P_2)/2$. The downstream capillary is used as a flow meter operating at a predetermined reference condition with an average pressure of $P_{3,4} = (P_3+P_4)/2$. The principle of the two capillary viscometer is based on the identical mass flow rates through both capillaries. The predetermined reference condition corresponds to a mass flow rate that has been gravimetrically calibrated in advance. Therefore, it is essential to keep the flow rate constant through both the upstream and downstream capillaries during the measurements. The mass flow calibration is discussed in section 3.1.

The capillary geometry parameters ($r$ and $L$) in the working equation are cancelled out as a result of the ratio measurement, except for the correction factors. For the ratio measurement, both helium and the test fluid need to be measured at the same conditions. The pressure drop must be accurately measured for each data point using the pressure sensors at the inlet and at the outlet of both capillaries ($P_1, P_2, P_3, P_4$). The new two-capillary viscometer is combined with a density meter for the density measurement. However, using density predicted by models can be an alternative for fluids for which there is available a sufficiently accurate equation of state.

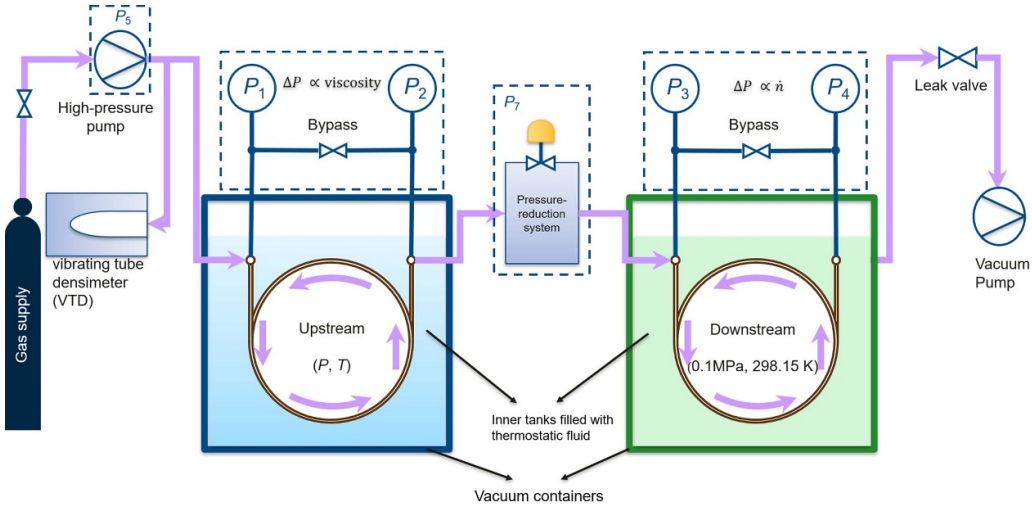


**Figure 2.** A simplified schematic of two- capillary viscometer.

The three main ratios $\left(\eta^{\mathrm{fld}}_{0,T_{\mathrm{ref}}}/\eta^{\mathrm{He}}_{0,T_{\mathrm{ref}}}\right)$, $\left(\eta^{\mathrm{He}}_{P,T}/\eta^{\mathrm{He}}_{0,T}\right)$, $\left(R^{\mathrm{fld,\,He}}_{T,T_{\mathrm{ref}}}\right)_{P,0}$ are determined experimentally as described in the following sections.

### 3.1. Downstream capillary as a flow meter

The reference ratio $\left(\eta^{\mathrm{fld}}_{0,T_{\mathrm{ref}}}/\eta^{\mathrm{He}}_{0,T_{\mathrm{ref}}}\right)$ is obtained using the working equation (25) once for helium and once for the measured fluid:

$$\frac{\eta_{0,T_{\mathrm{ref}}}{}^{\mathrm{fld}}}{\eta_{0,T_{\mathrm{ref}}}{}^{\mathrm{He}}} = \frac{\left[\rho\left(T,\bar{P}_{3,4}\right)\left(P_3-P_4\right)\mathrm{C}'_{\mathrm{Lp}}\left(T_{\mathrm{ref}},P_3,P_4\right)\right]^{\mathrm{fld}}}{\left[\rho\left(T,\bar{P}_{3,4}\right)\left(P_3-P_4\right)\mathrm{C}'_{\mathrm{Lp}}\left(T_{\mathrm{ref}},P_3,P_4\right)\right]^{\mathrm{He}}} \times \frac{\dot{m}^{\mathrm{He}}}{\dot{m}^{\mathrm{fld}}} \tag{33}$$

where subscripts 3 and 4 denote the inlet and outlet of the downstream capillary operating at the reference conditions. In this case, the downstream capillary is combined with a custom-made gravimetric setup operating as a flow meter to determine the mass flow rate of helium and the fluid during the experiment. The downstream capillary reference temperature is set at $T_{\mathrm{ref}} = 298.15$ K and the predetermined pressures $P_3$ and $P_4$ are low pressures, around 0.1 MPa. Helium or the fluid flows through the downstream capillary from a small portable sphere, filled with the helium or fluid in advance. The pressures $P_3$ and $P_4$ are maintained constant at predetermined values during the flow period. Hence, the unknown mass flow rate $\rho$ that has flowed through the downstream capillary is constant and can be accurately determined during the flow period t as:

$$\dot{m} = \frac{m_{\mathrm{before}} - m_{\mathrm{after}}}{t} \tag{34}$$

where $m_{\mathrm{before}}$ and $m_{\mathrm{after}}$ are the weight of the sphere with the fluid content before and after the flow measurement. Since the downstream capillary works at a low pressure of $\bar{P}_{3,4} = 0.1$ MPa, the correction factor at low pressure ($L_P$) is applicable.

### 3.2. Two-capillary viscometer: effect of pressure

The two-capillary viscometer can conduct viscosity measurements for both gases and liquids at high pressures. Yet, there are some differences in the technical details and methods for different phases. For example, the correction factor relevant to compressibility and slip factors must be considered only for the measurements of gases. On the other hand, measurements at high pressures require extreme attention to have the appropriate capillary material, secure the capillary position, create a constant fluid flow, and keep the pressure difference small enough. The capillary expansion due to the high temperature and pressure needs to be considered. The capillary expansion due to the high temperature and pressure needs to be considered.

Helium was used to investigate the effect of high-pressure on the ratio measurement. These one-time measurements of the ratio $\eta^{\mathrm{He}}_{P,T}/\eta^{\mathrm{He}}_{0,T}$ can be used as input for the measurements of different fluids at the same pressure and temperature measured for helium. During calibration with helium, both the upstream and downstream capillaries are maintained at the desired temperature $T$. The ratio $\eta^{\mathrm{He}}_{P,T}/\eta^{\mathrm{He}}_{0,T}$ is obtained by writing working equation (26) once for the upstream and once for the downstream and eliminating $\dot{n}$ due to identical flow:

$$\left(\frac{\eta^{\mathrm{He}}_{P,T}}{\eta^{\mathrm{He}}_{0,T}}\right) = \frac{Z_{\mathrm{down},T}(0)}{Z_{\mathrm{up},T}(P)} \frac{\left[\rho\left(T,\bar{P}_{1,2}\right)\left(P_1-P_2\right)\mathrm{C}'_{\mathrm{Hp}}\left(T,P_1,P_2\right)\right]^{\mathrm{He}}}{\left[\left(\rho\left(T,\bar{P}_{3,4}\right)\right)\left(P_3-P_4\right)\mathrm{C}'_{\mathrm{Lp}}\left(T,P_3,P_4\right)\right]^{\mathrm{He}}}. \tag{35}$$

To obtain the ratio measurement for helium, two experiments must be conducted. First, the upstream capillary is operated at the test pressure $P$ and the downstream capillary at the reference pressure. The correction term C′Hp for upstream capillary operating at a high pressure is defined by equation (26), where $g'^{\mathrm{virial,\,Hp}}\left(P_1,P_2\right) = 0$.

The second experiment is conducted at low pressure to determine the impedance ratio $\left(Z_{\mathrm{down},T}(0)/Z_{\mathrm{up}.T}(P)\right)$ in equation (35). Subscript 'up' and 'down' refer to the upstream

and downstream capillaries, respectively. The impedance $Z$ at a given temperature is:

$$Z(T) = \frac{16 L_T}{\pi {r_T}^4}. \tag{36}$$

To avoid using the nominal values for capillary inner diameter $r$ and length $L_T$ at the temperature of $T$, the impedance ratio at low pressure was defined as:

$$\begin{aligned}\frac{Z_{\mathrm{up},T}(P)}{Z_{\mathrm{down},T}(0)} &= \left[\frac{Z_{\mathrm{up},T}(P)}{Z_{\mathrm{up},,T}(0)}\right]\frac{Z_{\mathrm{up},T}(0)}{Z_{\mathrm{down},,T}(0)} \\ &= \left[\frac{Z_{\mathrm{up},T}(P)}{Z_{\mathrm{up},,T}(0)}\right]\frac{\left[\rho(T,\bar{P}_{\mathrm{min},1,2})(P_{1,\mathrm{min}}-P_{2,\mathrm{min}})\mathrm{C}'_{\mathrm{Lp}}(T,P_{1,\mathrm{min}},P_{2,\mathrm{min}})\right]^{\mathrm{He}}}{\left[\rho(T,\bar{P}_{3,4})(P_3-P_4)\mathrm{C}'_{\mathrm{Lp}}(T,P_3,P_4)\right]^{\mathrm{He}}}.\end{aligned} \tag{37}$$

Equation (37) need to be calculated for a minimum pressure $P_{\mathrm{min}}$ at the upstream capillary. Note that the correction used $\mathrm{C}'_{\mathrm{Lp}}$ is valid if achieved minimum pressure $P_{\mathrm{min}}$ is sufficiently low, otherwise $\mathrm{C}'_{\mathrm{Hp}}$ should be considered. This ratio is used for different pressure points as a reference point at one isotherm.

The axillary data of ratio $Z_{up,T}(P)/Z_{\mathrm{up}.T}(0)$ can be calculated from the dimensions and elastic modulus of the capillary due to the dilation of the capillary's inner diameter with pressure $Z_{up,T}(P)$ is defined as:

$$\frac{Z_{\mathrm{up},T}(P)}{Z_{\mathrm{up},T}(0)} = \frac{(1+\Delta Z_{0\to P}+\Delta Z_{298.15K\to T})}{(1+\Delta Z_{298\to T})} \tag{38}$$

where $\Delta Z_{0\to P}$ shows the pressure expansion of the capillary from zero to pressure of $P$. For measurement at different temperatures, the thermal expansion must be taken into consideration. One of the reasons for choosing the fused silica glass capillaries was the very low coefficient of thermal expansion of this material across all temperature ranges. The averaged thermal expansion coefficient is $0.57 \times 10^{-6}$ K$^{-1}$ from 273.15 K–473.15 K. Low thermal expansion coefficients allow for a very high resistance to thermal shock, making fused silica glass ideal for applications that experience temperature fluctuations. Comparatively, thermal expansion can be twenty times higher for a nickel-iron alloy. Applying the silica glass thermal expansion coefficient gives that impedance change due to the temperature $\Delta Z_{298.15K\to T}$ is $-1.016\ 421 \times 10^{-6}$ K$^{-1}$. For the pressure effect, the stresses in axial, circumferential and radial directions in the capillaries were investigated and a pressure expansion coefficient of $5.218 \times 10^{-5}$ MPa$^{-1}$ was obtained, (see appendix A). Therefore, the total effect of temperature and pressures up to 100 MPa for the quartz capillary are determined as:

$$\begin{aligned}(\Delta Z_{0\to P}+\Delta Z_{298\to T}) = &-1.02\times10^{-6}\mathrm{K}^{-1}(T-298.15\ \mathrm{K}) \\ &+5.23\times10^{-5}\mathrm{MPa}^{-1}\times P.\end{aligned} \tag{39}$$

### 3.3. Two-capillary viscometer: viscosity measurements

The viscosity measurements are performed to obtain the viscosity ratio, $\left(R^{\mathrm{fld,\,He}}_{T,T_{\mathrm{ref}}}\right)_{P,0}$ in equation (31). During the measurements, helium, and the measured fluid flow alternatingly through the two capillaries. In both cases, the upstream is kept at the target temperature and pressure, and the downstream capillary is maintained at reference conditions. It is important to keep the flow constant at the predetermined pressure drop $(P_3-P_4)$ and the reference temperature $T_{\mathrm{ref}}$ in the downstream capillary. The viscosity ratio, $\left(R^{\mathrm{fld,\,He}}_{T,T_{\mathrm{ref}}}\right)_{P,0}$, is then found from the ratio:

$$\left(R^{\mathrm{fld,\,He}}_{T,298}\right)_{P,0} = \frac{\left[\rho(T,\bar{P}_{1,2})(P_1-P_2)\mathrm{C}'_{\mathrm{Hp}}(T,P_1,P_2)\right]^{\mathrm{fld}}\left[\rho(T_{\mathrm{ref}},\bar{P}_{3,4})(P_3-P_4)\mathrm{C}'_{\mathrm{Lp}}(T_{\mathrm{ref}},P_4)\right]^{\mathrm{He}}}{\left[\rho(T_{\mathrm{ref}},\bar{P}_{3,4})(P_3-P_4)\mathrm{C}'_{\mathrm{Lp}}(T_{\mathrm{ref}},P_3,P_4)\right]^{\mathrm{fld}}\left[\rho(T,\bar{P}_{1,2})(P_1-P_2)\mathrm{C}'_{\mathrm{Hp}}(T,P_1,P_2)\right]^{\mathrm{He}}}. \tag{40}$$

Combining the results from sections 3.1–3.3 and the reference *ab initio* viscosity of helium [17] as done in equation (31) gives the viscosity value for the fluid under test at the desired temperature and pressure.

## 4. Experimental section

### 4.1. Material

The pure components used in this work are presented with information on suppliers and purity in table 1.

**Table 1.** Pure fluids used.

| Chemical | Supplier | Mole fraction purity, $x$ |
|---|---|---|
| $CO_2$ | Linde | 0.999 993 |
| He | Linde | 0.999 999 |

### 4.2. Experimental procedure

The capillaries were coiled and horizontally immersed in the thermostatic fluid inside two inner tanks, upstream and downstream. The operation of the process was carried out by the LabVIEW control and data acquisition program. However, several manual procedures were necessary. The thermostatic baths and inner tanks were filled with thermostatic fluid manually for example. Water was used as thermostatic fluid for the experiments reported in this work. The heating system comprises a hot bath, cold bath, external pumps, heating elements, and manual valves. The thermostatic fluid was circulated to efficiently control the temperature in the system. Four alternative configurations of the heating system are available such that each circulating bath could be used to regulate the temperature of the upstream capillary, the downstream capillary, both upstream and downstream capillaries, or not be used at all. Hence a correct configuration of the valves' settings was essential. In addition, the inner tanks were placed in vacuum-insulated outer containers for the high precision of temperature control and to avoid heat loss to the environment. A prevacuum and a turbo-molecular pump were used to evacuate the outer containers to high vacuum pressure. The vacuum pumps were continuously running to maintain the vacuum pressures inside the vacuumed containers.

A vacuum pressure in the order of $11 \times 10^{-7}$ kPa at room temperature was required. The same vacuum system was used to evacuate gas lines, high-pressure pump, and all pipes from and to pressure sensors, capillary tubes, valves, and the density meter. When changing the test fluid, the whole system was flushed with the new test fluid to dilute any previous fluid remaining in the capillaries, lines, and pump. The procedure of evacuation and flushing had to be manually repeated three times at least to reach vacuum pressure below $1 \times 10^{-4}$ kPa inside the system. After the final evacuation, the pump and lines were filled with the test fluid.

*4.2.1. Flow measurements.* The downstream capillary was utilized as a mass flow meter and, and it measured gravimetrically the flow for helium and the test fluid ($CO_2$). The weighing process was a manual operation. A custom-made gravimetric setup consisting of a digital mass comparator (RADWAG) placed inside a glass chamber with two identical portable spherical tanks were used. An ABBA scheme was followed for the weighing procedure to gain accurate results. Applying the ABBA mass method with a comparator reduces the influence of various error sources, including variable buoyancy and non-ideal repeatability/linearity of the scale. The principle of the ABBA scheme method is to compare the weight of two objects, A and B, and estimate the weight of the sample inside object B by the measured difference between the A and B. Objects A and B have the same volume to reduce the impact of varying buoyancy. In our case, the sphere containing the test fluid was object A, and the second empty sphere was considered object B.

The flow measurement procedure started with connecting the portable sphere A to the pressure reduction system (upstream of $P_3$) and filling it with the fluid under test. The maximum pressure that the sphere A can be exposed to is 4 MPa. After filling, it was ensured that sphere A reached the equilibrium temperature with the environment by monitoring the sphere temperature. The upstream pump kept the pressure constant until the sphere reached room temperature. Sphere A, containing gaseous fluid, was then disconnected from the system, transferred to the inside of the balance chamber, and kept there for a while before weighing. In total, the filling process and the waiting for reaching steady state took a few hours. The weighing procedure started with weighing objects A and B in the order of A, B, B, and A, and repeating the ABBA weighing scheme ten times. During weighing, it was crucial to make the weight of the two objects as equal as possible using accurately calibrated weights to minimize the impacts of non-linearity from the comparator. Before and after the ABBA weighing scheme, the chamber was closed, and the conditions, such as temperature, air pressure, and humidity inside the chamber, were recorded. After weighing, sphere A was re-connected to the system. Each time after connecting the sphere to the rest of the system, the tubing and components exposed to the air were evacuated.

The next step was preparing the downstream capillary to discharge the fluid from the sphere. The downstream capillary was set at the reference conditions, a temperature of 298.15 K, and constant predetermined low pressures $P_3$ and $P_4$. To maintain constant $P_3$ and .pressures, a high-pressure pump suppling fluid at a pressure of $P_7$ upstream of the downstream capillary. The pressure supplied by the high-pressure pump was the pressure inside the sphere.

When the pressure drop ($P_3$–$P_4$) along the downstream capillary was constant for at least 10 min, the downstream capillary was disconnected from the upstream and connected to the sphere by simultaneously closing and opening the corresponding valves. The flow period $t$ began when the valve from the sphere was opened.

The main component of the pressure reduction system is a control valve (V-26), shown in yellow in figure 2. The V-26 regulates the flow into the downstream capillary by

maintaining the pressure $P3$ constant. However, in practice, the actual flow resistance by the valve was found in between 10% (close) and 70% (open). During the flow measurements, the end of the flow period $t$ was defined as the time when V-26 was fully open (80%), which meant no resistance to flow. In that case, the valve connecting the sphere A was automatically closed. The flow measurement ended when the valve was closed. Then the sphere was weighted again to calculate the mass of the fluid that had flowed through the downstream capillary during the flow period $t$. The difference in the weight of the sphere before and after the flow measurement equals the unknown mass of test gas discharged during the flow period $t$. Flow calibration, as one-time measurement, was required for both helium and the test fluid.

*4.2.2. Viscosity measurements.* Viscosity was measured isotherm by isotherm because it takes long to heat and cool the containers. In this work, water was used as the thermostat fluid since it is suitable for the temperature range between 278.15 K and 353.15 K. The measurements were performed for five isotherms: 280.01 K, 298.15 K, 300.01 K, 323.15 K, and 348.15 K. Density, viscosity, and phase behaviour were estimated prior to the experiments to avoid measurements in the two-phase and solid-state regions. This was done for two main reasons. First, viscosity measurements in the two-phase region are meaningless. Second, for gas mixtures, the fluid must remain in a single gas phase region in all parts of the facility including, the pump, buffer tank, tubing, and capillaries. A phase transition would result in changes of the fluid composition. For measurements in the liquid phase, the phase transitions between liquid and gas were performed by keeping the temperature above the critical point.

According to equation (32), three measurements were required for each viscosity data point: ordinary measurement for the test fluid ($CO_2$), ordinary measurement for helium to determine $(R^{\mathrm{fld,\,He}}_{T,T_{\mathrm{ref}}})_{P,0}$, and a high-pressure calibration for helium $\left(\eta^{\mathrm{He}}_{P,T}/\eta^{\mathrm{He}}_{0,T}\right)$.

During an ordinary viscosity measurement, the upstream capillary was set at the measurement temperature $T$ and the downstream capillary was set at the reference temperature, 298.15 K. For the measurements at temperatures $T \geqslant 298.15$ K, the heating system was operated in the configuration when the hot bath was used for the upstream capillary and the cold bath for the downstream capillary. For the measurements at temperatures $T < 298.15$ K, the temperatures of upstream and downstream capillaries were both regulated by the cold bath. This was necessary to ensure that the temperatures of both upstream and downstream capillaries were stabilized before starting the measurements. A gas bottle was used to fill the system with the test fluid before starting the measurements. The inlet pressure of the upstream capillary $P1$ was regulated to the desired measurement pressure $P$ by the pump. The pump and the control valves regulate the corresponding variables based on a digital PID controller. The pressure of the downstream capillary was kept at an average pressure $\bar{P}_{3,4} = 0.1$ MPa. Both bypass valves were open to measure the bias between the pressure transmitters at the inlet and outlet of the capillaries. There must be no flow through the system during the bias measurements. Bias measurements were performed before and after each measurement point to increase the precision of the pressure drop measurement and lasted for a duration of time between 5 min and 10 min. There was an array of pressure transmitters with different operating pressure ranges. Depending on the operating pressure, the correct pressure sensor was used. The measurement was started by closing bypass valves, flowing the fluid through the capillaries by opening several valves at the inlet and outlet of upstream and downstream capillary and regulating the pressures $P_1$, $P_3$, and $P_4$. The high-pressure pump kept pressure $P_1$ constant, pressure $P_3$ was regulated by the reduction system (control valve V-26 and several auxiliary capillaries) and pressure $P_4$ was maintained constant using a leak valve. The reading output pressure of $P_2$ was used for the viscosity calculation. The data collection was conducted within the period that the pressure drops across the upstream and downstream capillaries were constant for at least 40 min.

However, the measurements at high pressure could take several hours to achieve a stable pressure drops $(P_1 - P_2)$ and $(P_3 - P_4)$ along the capillaries. The key factor ensuring stable pressure drops and thereby constant flow through the two-capillary viscometer was reaching a stable pressure between the upstream and downstream capillaries $P_7$. Stabilization of that pressure was a slow process in particular at high pressures, when it took several hours. V-26 could not regulate the flow at downstream capillary by itself at high pressures. Therefore, the auxiliary capillaries mounted in the pressure reduction system were used to increase the flow resistance and to reaches the target pressure $\bar{P}_{3,4}$ downstream. The above-described ordinary measurement procedure was repeated once for the CO2 and once for helium.

The helium high-pressure calibration was carried out in the same manner as the ordinary measurement, except that the upstream and downstream capillaries were set at the measurement temperature $T$.

Therefore, only one thermostatic bath, depending on the operating temperature, was used. Helium calibration measurements required operating the two-capillary viscometer in two modes: at a possible minimum pressure $P_{\mathrm{min}}$ and the pressure $P$, as explained in section 3.2. The results obtained for low-pressure measurement $P$min were used for all data points at one isotherm.

## 5. Uncertainty analysis

The two-capillary viscometer setup is aimed for accurate measurements for a wide range of pressures and temperatures. Therefore, sophisticated calibration procedures and routines were designed and followed to minimize and quantify the measurement uncertainty. Uncertainty analysis is conducted based on the general rules for evaluating and expressing uncertainties in the measurements provided by 'GUM' [18].

For the experimental viscosity data, the overall combined expanded uncertainty $U_c$is expressed, as equation (41):

$$U_c(\eta) = k.u_c(\eta) \tag{41}$$

where $k$ is the coverage factor [18]. The overall combined standard uncertainty $u_c(\eta)$ is determined from:

$$u_c(\eta) = \sqrt{\left[\left(\partial\eta/\partial T\right)_P u(T)\right]^2 + \left[\left(\partial\eta/\partial P\right)_T u(P)\right]^2 + \left[\left(\partial\eta/\partial x\right) u(x)\right]^2 + u(\text{model})^2} \tag{42}$$

where $u(T)$, $u(P)$, $u(x)$ and $u$(model) are the combined standard uncertainties of the temperature, pressure, composition, and the the working equation used for viscosity measurements, respectively. The uncertainty $u(x)$ in composition is applicable only for the viscosity measurements of fluids mixtures. The combined uncertainties include Type A (statistical analysis of measured quantity) and Type B uncertainties (by means other than a Type A evaluation of measurement uncertainty, for example calibration results or manufacturer's manuals). The Type B uncertainties of temperature and pressure were estimated separately through the calibrations. A good estimation for the standard uncertainty obtained from the calibration fit is from the statistical analysis provided as:

$$u(y) = \sqrt{\frac{\sum (y - y_{\text{calc}})^2}{n - p}} \tag{43}$$

where the standard uncertainties of the model used for each measured variable $y$ (temperature, pressure etc) is $u(y)$, $y_{\text{calc}}$ is the calculated value of $y$ from the calibrations, $n$ is the number of data points used for the model fit and $p$ is the degree of freedom of the model. Sophisticated calibration procedures and routines were followed to minimize and quantify the uncertainty of measurements. The temperature calibration standard ITS-90 was followed to calibrate standard platinum resistance thermometers (SPRTs) and PTs sensors. Pressure calibrations were also performed to estimate the uncertainty in pressure for different pressure sensors. The following sections will discuss the results of temperature and pressure calibrations and the factors contributing to the uncertainty for the viscosity data points.

### 5.1. Uncertainty in temperature measurements

Precise temperature measurement is important because the viscosity dependence on temperature is significant. In total six temperature sensors including two SPRT sensors with the nominal resistance of 25 Ω (Fluke-Model: SPRT 5686-B) and four PT100s sensors with the nominal resistance of 100 Ω (Fluke model: 5615-9-B) were used for the temperature measurements. All sensors were calibrated according to the temperature calibration standard ITS-90 (International Temperature Scale of 1990 [19]). It is recommended to use fixed-point cells for calibration of SPRTs since they are used as standard temperature sensors with higher accuracies. On the other hand, PT100s have larger uncertainties and for this reason a comparative calibration against a reference SPRT was applied. As the operating temperature for the viscosity measurements is in the range of 213.15–473.15 K, the ITS-90 calibration procedure was performed in three subranges: the triple point of mercury (T90 ≡ 234.3156 K), the triple point of water (T90 ≡ 273.16 K), the melting point of gallium (T90 ≡ 302.9146 K) and the freezing point of indium (T90 ≡ 429.7485 K). The heat source for the melting point of gallium to the freezing point of indium was a high temperature calibration oil baths (Fluke: model 6020) and for the triple point of mercury, a cold bath (Fluke: model 7080) was used.

The principle of fixed-point calibration is to determine the deviation of resistance $W(\text{T90})$ of the SPRT from ITS-90 reference resistance $W_r$ at ITS-90 temperatures (T90) using fixed-pint cells. Then, it will be possible to calculate the temperature by measuring the resistance of the SPRT at the unknown temperature and comparing this resistance to the measured resistance at other known temperatures. An extrapolation is needed for the temperatures higher than the freezing point of indium and lower than the triple point of mercury. However, as a general rule, it is recommended to avoid the extrapolation beyond the calibration range, unless an estimated uncertainty is introduced by extrapolating a deviation function. The resistance of the four-wire SPRTs was measured utilizing an ASL resistance thermometry bridge (CTR6500). The resistance ratio $W(\text{T90})$ is defined as:

$$W(\text{T90}) = \frac{R(\text{T90})}{R(\text{TPW})} = \frac{R(\text{T90})}{R(\text{bridge})} \times \frac{R(\text{bridge})}{R(\text{TPW})} \tag{44}$$

where $R(T90)$ is the measured SPRT resistance at the specified temperature and $R(\text{TPW})$ is the measured SPRT resistance at the triple point of water (TPW = 273.16 K). $R(\text{bridge})$ considers the internal resistance inside the thermometry bridge. In order to minimize the effect of self-heating, SPRTs resistance was measured for three different currents: 0.5 mA, 1 mA and 1.4 mA. The obtained results were extrapolated to zero current using a linear fit, where the maximum deviation of −86.75 mK at the freezing point of indium was observed. The estimated uncertainties for the fixed-point cells are given by the manufacturer, as reported in table B.1 in appendix B.

After the calibration for the three subranges, a linear fit between the ITS-90 temperatures for four fixed points and measured temperatures by SPRTs was used for the temperature calibration. The expanded combined uncertainty (by

coverage factor $k = 2$, providing a confidence level of approximately 95%) of 15 mK was achieved.

The PT100s have more significant uncertainties. Thus, performing a comparative calibration method against a reference SPRT is common. All PT100 sensors were simultaneously calibrated against the average temperature of both SPRTs. The maximum deviation of all four PT100s within the whole temperature range was 93.39 mK at the temperature of freezing point of indium. After calibrations, the maximum expanded combined uncertainty ($k = 2$) for all PT100 was 84 mK. The uniformity of temperature is included in the uncertainty estimations through the arithmetic mean values for the three upstream PT100s. During the calibrations and measurements, the temperature stability was around 10 mK.

### 5.2. Uncertainty in pressure measurements

Highly accurate pressure measurements are crucial because the pressure drop is approximately proportional to the viscosity for a laminar flow. As mentioned, an array of custom-made precision pressure transmitters with different full-scale pressures of 2.1 MPa, 6.9 MPa, and 13.8 MPa (Paroscientific), and 100 MPa (Keller) are used. The pressure transmitters also offer a 0.0005%FS (full scale) resolution. The pressure sensors were calibrated by the manufacturer with an absolute accuracy of 0.01%FS. However, a field calibration was necessary since the pressure sensors were four years old. The pressure sensors were calibrated in-house against a dead weigh tester, where three different piston cells with different pressure ranges and uncertainty were used. The estimated accuracy of piston cells reported by the manufacturer is presented in table C.1 in appendix C. The pressure calibrations were carried out within an interval of 10 months. The pressure sensors were calibrated horizontally as they operate during the measurements. The accuracy of the pressure sensors was checked by comparing results of two calibrations. The uncertainty of pressure sensors was limited by the deviation from the calibration function defined using a second-order polynomial fit and the deviation between the results of two calibrations. Pressure uncertainties of 0.000 25 MPa, 0.000 43 MPa, 0.0022 MPa and 0.0057 MPa for pressure up to 2.1 MPa, 6.9 MPa, 14.8 MPa and 100 MPa were estimated. Table C.2 in appendix C presents the uncertainty of each pressure sensor.

### 5.3. Uncertainty of the viscosity model

Various sources contribute to the uncertainty of viscosity measurements, as defined in equations (25) and (31)–(40). The reference viscosity $\eta^{\mathrm{He}}_{0,T_{\mathrm{ref}}}$ and the ratio viscosity $\left(\eta^{\mathrm{He}}_{0,T}/\eta^{\mathrm{He}}_{0,T_{\mathrm{ref}}}\right)_{abinitio}$ are the two contributions determined from *ab initio* calculation, both with a relative uncertainty of 0.01%. The uncertainty of measured viscosity is a combined uncertainty due to several factors, depending on flow measurements, pressure drop and other contribution such as parameters used in the correction factors.

*5.3.1. Pressure drop.* Errors in the pressure drop have a significant impact on the uncertainty of measurements as the viscosity is proportional to the pressure drop. The array of different pressure sensors enhances the accuracy of the pressure measurements. For accurate measurements, the bias measurements should be performed before and after each measurement. The final bias measurement is an arithmetic average of results for the bias measurement before and after each experiment. Appendix D describes the derivation of the uncertainty in pressure drop. The final expression is given as:

$$u^2_{\Delta P} = u^2_{\mathrm{r}} + \Delta P^2 u^2_{\mathrm{B}} \tag{45}$$

where $u\,(\Delta P)$ is the total uncertainty in pressure drop $\Delta P$, $u\,(er)$ can be found from the repeatability of the measurement and the dimensionless uncertainty $u_{\mathrm{B}}$ due to the bias of the pressure gauge is given by:

$$u_B = \frac{U(P_{\max})}{P_{\max}} \tag{46}$$

where $U(P_{\max})$ is the uncertainty of each pressure sensor determined from the pressure calibration at the maximum pressure $P_{\max}$. Test operations for helium were performed to check the repeatability of the pressure drop, which significantly impacts the measurements. Helium flowed through the capillaries with the inner diameters of 200 μm and 500 μm at upstream and downstream, respectively. To quantify the repeatability of the viscometer, three test measurements at different pressures (up to 20 MPa, in this work) were repeated. The repeatability was 0.33%, 0.23% and 0.04%, at high, medium, and low pressures, respectively, as shown in table 2.

*5.3.2. Error in the working equation.* As discussed in section 2.3, for simplicity, $(P)$ was assumed to be a linear function of $P$. However, for accurate measurements, it is important to justify this assumption by estimating the associated error. We need to show that $\varepsilon\,(P)\,\Delta P^2$ in equation (23). is small. The data calculated using NIST REFPROP 10.0 database [14], were used to estimate the density and viscosity of CO2 for the calculation of $(P)$. A numerical approximation was used for the second derivative:

$$\frac{\partial^2 \xi\,(P)}{\partial P^2} = \frac{\xi\,(P+\Delta P) - 2\xi\,(P) + \xi\,(P-\Delta P)}{\Delta P^2}. \tag{47}$$

A maximum relative uncertainty of 1% was estimated for the $\Delta P$. Figure 3 shows the normalized quantity $(P)\,\Delta P^2$ as a function of pressure $P$. The maximum value of ten occurs close to the critical point of $CO_2$ at $T = 304.13$ K and $P = 7.38$ MPa, where the sensitivity of density and viscosity to pressure is significant. Therefore, at that point and for a pressure difference of $\Delta P = 0.01\ P$, the value of the dimensionless error term in equation (23) will be only 0.001. The values at other points are 10 times smaller, so that the values of $(P)$ calculated by the working equation (26) will have a maximum error due to the linear approximation of no more than 0.01%.

**Table 2.** The repeatability of the two-capillary viscometer for helium at high, medium, and low pressures where $\bar{\boldsymbol{P}}_{3,4} = 100$ kPa and $\Delta \boldsymbol{P}_{3,4} = 30$ kPa.

| $T$/K | Pressure sensor used in E-07 | $P$/MPa | $(\Delta P_{1,2}/\Delta P_{3,4})_{\text{average}}$ | Standard deviation $u$/MPa | Repeatability/% |
|---|---|---|---|---|---|
| 298.15 | PS11-PS21 | 18.00 | 3.202 | 0.0106 | 0.33 |
| 298.15 | PS14-PS24 | 11.10 | 2.019 | 0.0047 | 0.23 |
| 313.11 | PS13-PS23 | 3.00 | 3.1815 | 0.0009 | 0.04 |

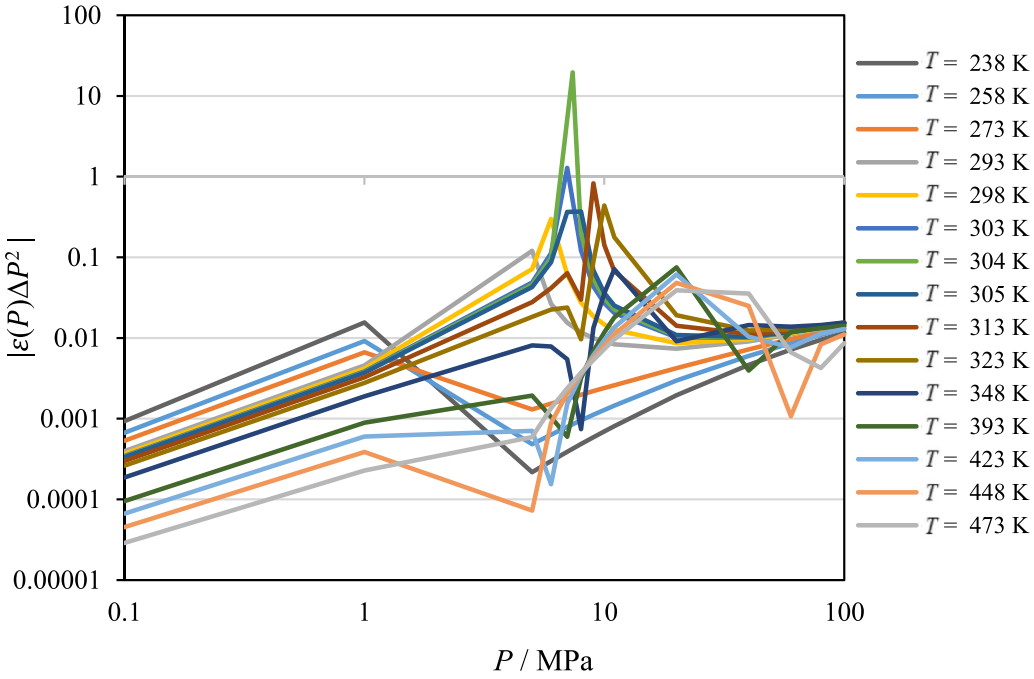


**Figure 3.** $\varepsilon(\boldsymbol{P})\,\boldsymbol{\Delta P}^2$ for $CO_2$ based on NIST REFPROP 10.0 database [14] over different temperatures ranges from 238 K to 473 K.

*5.3.3. Leakage.* A small leakage during measurements contributes to errors in the measurements. A helium sniffer was used to detect the location of leakage by measuring thermal conductivity which depending on the composition of the gas. This was an effective method for small leakages because helium leakage rates of the order of $10^{-6}$ Pa·m$^3$ s$^{-1}$ are normally detected by the helium sniffer. Based on the Graham laws of diffusion [20], the rate of diffusion for a gas is inversely proportional to the square-root of its molecular mass. Therefore, helium is a good candidate due to several of its features; is the lightest, fastest and a safe and non-flammable gas. Additionally, helium is the main working fluid as the reference. Repairing the location of leakage for helium improved the system for other test fluids. The leakage tests were investigated in two steps: the initial tests and the final tests. The initial leakage tests were done to ensure that no single component or connection suffer from leakage. The potential for leakage was checked by a simple test setup consisting of a pressure sensor, temperature sensor, and a high-pressure pump. The idea of the test setup was to enclose a small volume of some fluid at very high pressure (∼100 MPa) and detect whether any leakage occurs. The advantage of having a test setup was to have less complexity in comparison to the main setup. It was also easier to connect/disconnect the components for testing/repairing the test setup. This approach minimized the risk of damaging the main setup during the initial tests. The test setup was connected to the components to be leakage tested for leakage, such as valves, capillaries, pressure sensors. The high-pressure pump was used to raise the pressure of the system. By reading the temperature and pressure of the system over long-time periods, typically overnight tests, small leakage rates were detected as reduced pressure within the system. The final leakage tests were done after the main facility was assembled. Due to the complexity of the rig, the leakage tests were done part by part. To consider the effect of room temperature fluctuations in the pressure changes, the mass loss rate was estimated by:

$$\rho = \rho(T,P) \tag{48}$$

$$\mathrm{d}\rho = \left(\frac{\mathrm{d}\rho}{\mathrm{d}T}\right)_P \mathrm{d}T + \left(\frac{\mathrm{d}\rho}{\mathrm{d}P}\right)_T \mathrm{d}P \tag{49}$$

$$\frac{\mathrm{d}m}{\mathrm{d}t} = V\frac{\mathrm{d}\rho}{\mathrm{d}t} = V\left(\left(\frac{\mathrm{d}\rho}{\mathrm{d}T}\right)_P \frac{\mathrm{d}T}{\mathrm{d}t} + \left(\frac{\mathrm{d}\rho}{\mathrm{d}P}\right)_T \frac{\mathrm{d}P}{\mathrm{d}t}\right) \tag{50}$$

where $m$ is mass loss due to the leak over the time $t$. The temperature and pressure dependency of density are $\left(\frac{\mathrm{d}\rho}{\mathrm{d}T}\right)$ and $\left(\frac{\mathrm{d}\rho}{\mathrm{d}P}\right)$, respectively, taken from NIST REFPROP 10.0 database [14]. $V$ is the volume of the system estimated through the

volume calculations. Gas diffusion through the walls of the quartz capillaries is most likely negligible [16]. The mass loss was considered a leakage and counted in the uncertainty estimation. A major helium diffusion was identified through the PTFE gasket of the pressure sensor, which was the main reason for setting the limit for the measurements to 20 MPa within this work.

## 6. Results and discussions

### 6.1. Estimated uncertainty in viscosity

Uncertainty analysis was conducted based on 'GUM' guide to the uncertainty of measurements [18]. The overall combined standard uncertainty $u_c(\eta(T,P))$ for pure $CO_2$ was determined from:

$$u_c(\eta) = \sqrt{\left[\left(\partial\eta/\partial T\right)_P u(T)\right]^2 + \left[\left(\partial\eta/\partial P\right)_T u(P)\right]^2 + u(\text{model})^2} \tag{51}$$

where $u(T)$, $u(P)$ and $u$(model) are the standard uncertainties of the temperature, pressure, and the model defined for viscosity measurements, respectively, for pure CO2. Table 3 presents the budget for the expanded combined uncertainty in a viscosity data point at the temperature of 323.15 K and pressure of 10.09 MPa as an example.

As could be seen, the major contribution to the uncertainty arose from the uncertainty in the measured viscosity. Contributions to the uncertainty in viscosity include ordinary measurements for the $CO_2$ at ($T$, $P$), ordinary measurements for helium at ($T$, $P$), and calibrations for helium; He ($T$, $P$) and He ($T$, $P_{\min}$). For each data point, there are eight sources for $\Delta P$, six sources for density ρ and two sources for mass flow measurements: $\dot{m}_{CO_2}$ and $\dot{m}_{He}$.

In addition, The uncertainties arising from the reference viscosity $\eta^{He}_{0,T_{ref}}$, the ratio viscosity $\left(\eta^{He}_{0,T}/\eta^{He}_{0,T_{ref}}\right)_{ab\,initio}$ and the correction factor C (viscosity virial coefficients, $K_{slip}$, $K_{ent}$, $K_{exp}$, estimated viscosity, thermal conductivity, $r$ and $L$) need to be considered as well. The term $u$ (E) used in the equation (52) represents the small contribution of all these parameters. The error due to the simplicity of working equation is another source of uncertainty of the measured viscosity. Therefore, the measured viscosity is a combined uncertainty, expressed as:

$$u(\text{model}) = \sqrt{\left[\left(\partial\eta/\partial(\Delta P)\right)u(\Delta P)\right]^2 + \left[\left(\partial\eta/\partial\rho\right)u(\rho)\right]^2 + \left[\left(\partial\eta/\partial\dot{n}\right)u(\dot{n})\right]^2 + [u(\text{E})]^2 + [u(\varepsilon(P)P^2)]^2}. \tag{52}$$

Table 4 presents an example for the expanded combined uncertainty budget at a temperature of 323.15 K and a pressure of 10.09 MPa for $CO_2$ using the two capillary viscometer.

The new two-capillary viscometer was intended to measure the accurate viscosity data. Errors in the pressure drop along upstream capillary at test conditions are major contributors to the total uncertainty. The main reason for the high uncertainty was the relatively low pressure drop across the upstream capillaries due to low mass flow rates, 41.944 μg $s^{-1}$ for helium and 615.552 μg $s^{-1}$ for $CO_2$, corresponding to $P_3 = 0.115$ MPa and $P_4 = 0.085$ MPa at the downstream capillary. In this work, capillaries with the inner diameter of 200 μm and 500 μm were used upstream and downstream, respectively. For future work, it is recommended to operate the two-capillary viscometer using smaller inner dimeter capillary at upstream to increase the pressure drop across the capillaries. Operating at higher flow rates and a different choice of reference fluid can potentially increase the pressure drop. However, the Reynolds and Dean numbers need to be carefully checked.

To reduce the systematic error due to the pressure sensors, each measurement should start and end with the bias measurements for pressure difference recorded by the same pressure sensors. An arithmetic average value of bias measurements was deducted from the main pressure drop measurements for both upstream and downstream capillaries. This approach is recommended to correct pressure drop by 'taring' the pressure differences reading from the identical sensors [11]. The stability of pressure reading for upstream capillary was checked through the bias measurements over a period of nine months that the measurements were performed. Standard deviations of 0.014 kPa, 0.04 kPa, and 0.046 kPa between pressure sensors (PS13 & PS23), (PS14 & PS24), and (PS11 & PS21) placed in E-07 were found, respectively. Standard deviation of 0.016 kPa was observed for the downstream capillary with the average pressure of 0.1 MPa. In addition, random errors due to the instability in reading pressure differences during the experiments must be added to the uncertainty of measurements because each experiment requires several hours. Our results show that Paroscientific sensors give a wider range of noise than those from Keller sensors although an opposite behaviour was expected.

In addition, the relative uncertainty of 0.14% from the mass flow measurements for helium has a significant impact on the total uncertainty. The accuracy of gravimetrical mass flow calibration could be improved by using reference gas with higher molecular weight with known and accurate reference viscosity. N2 and Ar can be potential candidates since their accurate reference viscosities are already available in the literature [21].

In this work, the density of CO2 was estimated using Span and Wagner equation of state [22] where at pressures up to 30 MPa and temperatures up to 523 K, the estimated uncertainty in density for CO2 ranges from 0.03% to 0.05%. For helium, between 200 K and 500 K, the uncertainty in density from the Helmholtz equation of state [23]

**Table 3.** Budget for the expanded combined uncertainty in viscosity at $\boldsymbol{T}=323.15$ K and $\boldsymbol{P}=10.094$ MPa for $CO_2$. $\boldsymbol{U_c}$ ($\boldsymbol{k}=2$) is the overall expanded standard uncertainty with 95% level of confidence ($k=2$).

| Source of uncertainty $f$ | Uncertainty | Coverage factor ($k$) | Sensitivity coefficient $\partial\eta/\partial f$ | Standard uncertainty $u\,(f)$ /μPa·s |
|---|---|---|---|---|
| Temperature ($T$) | 0.084 K | 2 | −0.980 | 0.041 |
| Pressure ($P$) | 0.011 MPa | 2 | 7.367 | 0.042 |
| Model) | 0.33 μPa·s | 2 | 1 | 0.164 |
| Combined expanded uncertainty $U_c$ ($k=2$) | | | | 0.35 μPa·s |

**Table 4.** Combined expanded uncertainty $\boldsymbol{U_c}$ ($\boldsymbol{k}=2$) at $T=323.15$ K and $P=10.09$ MPa for $CO_2$, with the viscosity of 28.557 μPa·s.

| Source of uncertainty ($f$) | Standard uncertainty/ μPa·s | Relative standard uncertainty $u(f)$/% | Sensitivity coefficient $\frac{\partial\eta}{\partial f}\frac{f}{\eta}$ | Relative standard uncertainty $u(\eta)$/% |
|---|---|---|---|---|
| **Mass flow rate/μg/s:** | | | | |
| $\dot{m}_{CO_2}$/mass flow of $CO_2$ | 0.0051 | 0.02 | −1.000 | 0.02 |
| $\dot{m}_{He}$/mass flow of helium | 0.0398 | 0.14 | 0.996 | 0.14 |
| **Pressure drop/kPa:** | | | | |
| $(\Delta P_{1,2})^{CO_2}$-ordinary measurement | 0.0914 | 0.32 | 1.000 | 0.32 |
| $(\Delta P_{3,4})^{CO_2}$-ordinary measurement | 0.0029 | 0.01 | −1.000 | 0.01 |
| $(\Delta P_{1,2})^{He}$-ordinary measurement | 0.0911 | 0.32 | −0.997 | 0.32 |
| $(\Delta P_{3,4})^{He}$-ordinary measurement | 0.0029 | 0.01 | 1.000 | 0.01 |
| $(\Delta P_{1,2})^{He}$-calibration measurement | 0.0914 | 0.32 | 1.000 | 0.32 |
| $(\Delta P_{3,4})^{He}$-calibration measurement | 0.0029 | 0.01 | −1.000 | 0.01 |
| $(\Delta P_{min,1,2})^{He}$ -calibration measurement | 0.0029 | 0.01 | −1.000 | 0.01 |
| $(\Delta P_{min,3,4})^{He}$-calibration measurement | 0.0029 | 0.01 | 1.000 | 0.01 |
| **Density/kg/m$^3$** | | | | |
| $\rho_m^{CO_2}(T,\bar{P}_{1,2})$-ordinary measurement | 0.0036 | 0.03 | 0.501 | 0.013 |
| $\rho_m^{CO_2}(T_{ref},\bar{P}_{3,4})$-ordinary measurement | 0.0041 | 0.03 | −0.575 | 0.014 |
| $\rho_m^{He}(T,\bar{P}_{1,2})$-ordinary measurement | 0.0021 | 0.02 | −0.500 | 0.008 |
| $\rho_m^{He}(T_{ref},\bar{P}_{3,4})$-ordinary measurement | 0.0025 | 0.02 | 0.575 | 0.009 |
| $\rho_m^{He}(T,\bar{P}_{1,2})$-calibration measurement | 0.0021 | 0.02 | 0.500 | 0.008 |
| $\rho_m^{He}(T,\bar{P}_{3,4})$-calibration measurement | 0.0049 | 0.02 | −0.575 | 0.017 |
| **Error from working equation** $\varepsilon(P)\,\Delta P^2$ | 0.00003 | 0.0001 | 1 | 0.0001 |
| **Other contributions:** $K_{slip}$ for $CO_2$ and helium,$K_{ent}$, $K_{exp}$, virial coefficients, thermal conductivity, $r/L$, $\delta$, $\eta_{0,T_{ref}}^{He}$, $\left(\eta_{0,T}^{He}/\eta_{0,T_{ref}}^{He}\right)_{ab\ initio}$ | 0.028 | | | 0.12 |
| Root sum of squares | 0.17 | | | 0.59% |
| Combined expanded uncertainty $U_c$ ($k=2$) | 0.33 | | | 1.17% |

is 0.03% up to pressures of 40 MPa. Reference viscosity $\left(\eta^{\mathrm{He}}_{0,298.15}\right)_{ab\,initio} = 19.8253\ (2)$ μPa·s and ratio viscosity $\left(\eta^{\mathrm{He}}_{0,T}/\eta^{\mathrm{He}}_{0,T_{298.15}}\right)_{ab\,initio}$ calculated *ab initio* by Cencek *et al* [17] with uncertainty of 0.01% were used for the uncertainty estimation. Calibrations against the reference viscosity for helium show a deviation of 4% from the nominal values of $r$ and $L$. Thermal conductivity was estimated with uncertainty of 5% for CO2 [24] and helium [25]. An uncertainty of 7% for $K_{\mathrm{ent}}$ was estimated based on the calculation for entrance correction $f_{\mathrm{e}} = 1 + \left[1 + 2.8(d + 2L_{\mathrm{e}}/L)^{1/3}\right]$ when the entrance length $L_{\mathrm{e}} = 0.06Re\ (d/L)$ [20] was defined for each capillary. The results were consistent with the spread of data reported in Kawata *et al* [26]. Uncertainty of 10% was considered for the slip correction based on the data reported and analysis performed by Berg [16], $u(K_{\mathrm{slip}}) = 0.1$.

### 6.2. Evaluation of the correction term

Based on the design of the experimental set up, the correction factors named in equation (5), were applied to all measured data to ensure the highest possible accuracy of the viscosity data. The second term in the bracket of equation (5), which includes five correction terms, describes the total flow as a sum of flows due the different terms (corrections A–E). The term $f_{\mathrm{cent}}$ is a multiple to the bracket, which means that the centrifugal factors correct for the sum of flows for $N$ number of coils.

The relative size of the corrections for the downstream capillary working as a flow meter is presented in the previous work [10]. For the upstream capillary, the budget of correction factors differs from the ones at the downstream capillary since the radius, length and the fluid properties are different. Maximum Reynolds number of 338 was observed for $CO_2$ due to the higher molar flow rate, indicating that the measurements were performed within the laminar flow regime. The ratio $r/L$ was in the order of magnitude $10^{-6}$ for the upstream capillary and has shown only a very small temperature dependency. The correction coefficients and the effects of the various correction terms are presented in more detail in the following paragraphs.

The $g'_{\mathrm{virial}}$ term includes the virial coefficients for viscosity at only low densities, mainly for the downstream capillary. The virial coefficients can be estimated by representing the experimental viscosity data using a linear or quadratic form of a power series in density or pressure. In this approach, the zero density viscosities are determined by extrapolating the linear or quadratic function to the zero density or pressure, as shown in equation (13). Hence, using accurate experimental viscosity data increases the accuracy of the estimated virial coefficients used in $g'_{\mathrm{virial}}$ and consequently, the accuracy of measured viscosity data. Since the viscosity measurements within this work spanned high-pressure ranges, the obtained results could not be used to determine the virial coefficients experimentally.

For CO2, one of the reliable sources is the data from Schäfer [27], who measured CO2 viscosity at low pressures with the relative uncertainty of 0.2%. Vogel [28] evaluated this data set and determined the reference viscosity $\eta^{\mathrm{CO2}}_{0,298.15} = 14.888$ μPa·s using a linear extrapolation. However, our investigation has revealed that the choice of extrapolation method significantly affects the reference viscosity value of CO2. When a second-order polynomial fit is used, the reference viscosity value obtained is $\eta^{\mathrm{CO2}}_{0,298.15} = 14.888$ μPa·s, which is slightly higher than the value reported by Vogal [28]. Although the difference between the two values is within the uncertainty of the experimental data, the value obtained from the second-order polynomial fit is more consistent with the values calculated from *ab initio* [17], Hendl *et al* [29] and the data from our own investigation [10].

For helium where the downstream capillary was operated at 298 K, viscosity data for helium from Gracki *et al* [30] was used to estimate the virial coefficients. However, calibration measurements at different temperatures presented a challenge, as finding experimental data that matched the isotherms used in this study was difficult. As a result, estimated viscosity data for helium from NIST REFPROP 10.0 database [14] were used instead to estimate virial coefficients.

Comparisons between the measured viscosity of CO2 in this study at 298 K showed that the choice of the viscosity virial coefficients from Gracki *et al* [30] or NIST REFPROP 10.0 database [14] had an impact of 0.09% on the flow rate deviation.

This shows the need for accurate experimental viscosity data for helium at low pressure and for different isotherms to improve the accuracy of the results.

*Slip correction:* The slip correction term corrects for the velocity of the gas at the capillary wall, which is not equal to zero. Slip increases the flow rate. The slip coefficient $K_{\mathrm{slip}}$ is equal to the ratio between the slip length and the molecular mean free path. $K_{\mathrm{slip}}$ has a value close to, but not necessarily equal to 1. The slip correction factor was considered for the gas phase measurements because the mean free path at lower densities becomes similar in size to the inner diameter of the capillary. In a liquid phase, the molecules are continuously colliding with their neighbors and the slip correction is not defined. In this work, the slip correction factor $K_{\mathrm{slip}} = 1.18$ was used as Berg [16] tested the impact of the slip correction by conducting flow measurements in the ranges $0 < Kn < 0.002$ for the glass material. The Knudsen number does not exceed 0.0009 for helium in this work. For CO2, the slip coefficient of 1.03 (4) with the accommodation coefficient of 0.993 (2) reported by Sharipov [31] was used. However, previous works considered a complete momentum accommodation and $K_{\mathrm{slip}} = 1.00$ for gases in quartz and nickel capillaries, except for helium. This choice gives a corresponding uncertainty of 0.002% in viscosity. Slip correction term depends on Knudsen number, which is proportional to the parameters; $\eta(T, P)$, $T^{1/2}$ and $1/P$, see equation (6). The maximum Knudsen number of 0.001 06 was seen when the downstream capillary was operating at highest temperature (348 K) and lowest pressure (0.1 MPa) for helium calibration measurements. The effect of slip correction terms on the flow rate was in a range of 0.5%–0.55% for all data points.

*Entrance correction:* Referring to the assumption in the Hagen–Poiseuille equation, the flow velocity along the axis of a tube is constant and has a parabolic profile across the

cross-section. The kinetic energy rises at the entrance of the capillary due to the reduced fluid flow from a $T$-piece into the capillary tube with a smaller inner diameter. The change in kinetic energy leads to a small pressure drop, which influences the measurements. A relatively good model for the entrance correction can be found in Kawata *et al* [26]. According to the estimation made in this wok $(1+2.8\,(1+0.12Re/L)^{1/3}$, for the maximum Reynolds number ($Re = 577$) using the new two-capillary viscometer, $K_{\text{ent}}$ is a value between 1.06–1.13. Berg [16] also showed for $100 < Re < 1500$, $K_{\text{ent}} = -1.14$, in accordance with earlier results [16], and for $Re < 100$, $K_{\text{ent}}$ is negligible. In this work, Reynolds number does not exceed 339. An effect of about 0.06% reduction in the flow rate was observed for CO2 in the liquid phase. The effects of the kinetic energy changes were negligible for the helium measurements. In addition, a transition from uniform to parabolic velocity profile in a straight capillary occurs near the entrance of the capillary over a distance called entrance length. An approximate estimation of the entrance length is obtained from $(0.02\ Re \cdot r)$ [32]. This approximation can be used for a coiled capillary as well [33]. The estimated entrance length was less than 0.006% of the capillary length of the upstream capillary, where the Reynolds number is high. The range of the Reynolds number in this work shows that the flow stayed within the laminar flow region during all measurements.

*Thermal correction:* An expression for thermal correction is presented in equation (48) in [16]. The effect of this correction is in the order of maximum $10^{-5}$.

*Expansion correction:* The kinetic energy increases due to the pressure reduction, resulting in gas expansion along the capillary. The expansion coefficient, $K_{\text{exp}} = 1$. However, the expansion correction is above one because the gas expansion distorts the velocity profile from the assumed fully developed parabolic profile. The contribution of the expansion correction to the uncertainty of viscosity is less than 0.002%. The maximum effect of expansion correction was seen for $CO_2$ in the downstream capillary with $-0.01\%$ effect on the flow. Generally, the expansion correction is likely smaller for a liquid than the gas.

The expansion correction is likely smaller for a liquid because the correction derived by van den Berg *et al* was for a compressible gas. The thermal correction may be larger because the friction heating is much larger than the expansion cooling. Those two effects approximately cancel each other in a nearly ideal gas but not in a liquid. An accurate analysis of these estimations is difficult. and requires further studies.

*Centrifugal effects:* The curved effect of coiled capillaries is corrected by $f_{\text{cent}}$, defined in the model as dependent on the Dean number. For both ordinary and calibration helium measurements, the centrifugal factors were equal to one. On the other hand, for $CO_2$ at upstream capillary, where Reynolds number and consequently Dean number are high, the centrifugal effect has an impact of $-0.01\%$ on the flow. Higher flow rates will substantially increase centrifugal effects.

### 6.3. Pure $CO_2$ viscosity measurements

The performance of the two-capillary viscometer was verified by conducting viscosity measurements of pure $CO_2$. The results of these viscosity measurements for pure $CO_2$ are presented in table 5. The in total 40 viscosity data points were measured at five isotherms: 280.01 K, 298.15 K, 300.01 K, 323.15 K, and 353.15 K and over a wide range of pressures, between 2 MPa and 20 MPa. Pure $CO_2$ was chosen as the test fluid since the two-capillary viscometer will be used to address the lack of experimental data for pure $CO_2$ and $CO_2$–rich mixtures.

The absolute viscosity data for pure CO2 are plotted versus the pressure in figure 4. As could be seen, the viscosity positively correlates with the pressure. Significant viscosity change occurs after phase transition, for example, from $T = 298$ K in a gas phase at pressures below 6 MPa to a liquid state above 6.5 MPa. The critical point of $CO_2$ is at $T = 304.13$ K and $P = 7.38$ MPa.

### 6.4. Comparison with earlier work

The measured data of this work were compared with different literature sources available for the viscosity of pure CO2 and the data calculated using the reference correlation [13]. The experimental data used for comparison purpose are listed in table 6. The literature sources are categorized into the primary data and secondary data in this work. The primary data were employed in developing the reference correlation [13] and identified as reliable measurements obtained from the instruments with high precision and a complete working equation. The other sources available in the literature are the secondary data. Both data sets were used for comparison and consistency check of data obtained this work using the new two-capillary viscometer and modified hydrodynamic model. Relative deviations of viscosity data measured within this work and data from the literature are plotted as a function of pressure in figure 5. The baseline for the comparison is the data calculated using the correlation for pure CO2, implemented in NIST REFPROP 10.0 database [14].

For the comparisons made in figure 5, the isotherms at 280 K, 298.15 K (at pressures above 6 MPa) and 300.15 K present data measured in the liquid phase. The baseline correlation was established based on the primary data sets from Vesovic *et al* [41], Michels *et al* [35], and van der Gulik [38] such that the data have consistency of $\pm 2\%$. Data published before 1990 was analysed by Iwasaki and Takahashi [37] and systematic deviations between data sets were identified. Currently, the data set of van der Gulik [38] from 1997 with an uncertainty of 1% is the most reliable data set for the liquid phase. The results from this study agree with the reliable data of Van der Gulik [38]. For the isotherms at 280 and 300 K, a maximum deviation of $\pm 0.5\%$ from the model [13] was seen for the measured viscosity in the liquid phase. The data from

**Table 5.** Experimental viscosity data, $\boldsymbol{\eta_{exp}}$, for pure $CO_2$ where $\boldsymbol{T}$ is the temperature, $\boldsymbol{P}$ is the pressure, $\boldsymbol{\rho_{calc}}$ is the density calculated from Span–Wagner EoS [22] implemented in NIST REFPROP 10.0 database [14], $\boldsymbol{\eta_{calc}}$ is the viscosity calculated using the reference correlation for pure $CO_2$ implemented in NIST REFPROP 10.0 database [11], and $\boldsymbol{U_c}(\boldsymbol{\eta})$ is the expanded combined uncertainty (k = 2) in viscosity.

| $T$/ K | $P$/MPa | $\rho_{calc}$ / kg m$^{-3}$ | $\eta_{exp}$ / μPa·s | $U_c(\eta)$/μPa·s ($k = 2$) | $100 \times (\eta_{exp} - \eta_{calc}) / \eta_{calc}$ | Phase[a] |
|---|---|---|---|---|---|---|
| 280.013 | 5.753 | 902.054 | 93.844 | 1.0829 | 0.53 | SL |
| 280.012 | 7.474 | 918.385 | 98.169 | 1.0829 | 0.51 | SL |
| 280.011 | 8.987 | 930.697 | 101.443 | 1.1246 | 0.33 | SL |
| 280.017 | 11.029 | 945.198 | 105.422 | 1.1793 | 0.06 | SL |
| 280.014 | 14.417 | 965.683 | 112.092 | 1.2443 | 0.29 | SL |
| 280.009 | 18.284 | 985.343 | 118.939 | 1.3006 | 0.44 | SL |
| 298.152 | 1.988 | 39.505 | 15.142 | 0.1492 | −0.31 | SG |
| 298.153 | 3.009 | 64.322 | 15.402 | 0.1595 | −0.36 | SG |
| 298.149 | 4.006 | 93.533 | 15.815 | 0.1678 | −0.34 | SG |
| 298.147 | 5.461 | 154.241 | 17.022 | 0.1841 | −0.27 | SG |
| 298.153 | 7.546 | 763.312 | 65.605 | 0.7391 | 0.55 | SL |
| 298.150 | 11.100 | 833.949 | 77.428 | 0.8671 | −0.65 | SL |
| 298.243 | 18.082 | 900.698 | 92.716 | 1.0682 | −0.12 | SL |
| 300.010 | 6.772 | 685.823 | 53.961 | 0.6879 | −0.16 | SL |
| 300.010 | 7.360 | 727.143 | 59.481 | 0.6870 | −0.45 | SL |
| 300.011 | 8.001 | 753.073 | 63.595 | 0.7217 | −0.12 | SL |
| 300.010 | 8.980 | 780.399 | 67.985 | 0.7663 | −0.20 | SL |
| 300.010 | 11.513 | 825.761 | 76.141 | 0.8596 | −0.28 | SL |
| 300.010 | 13.011 | 844.888 | 80.082 | 0.9191 | −0.13 | SL |
| 300.010 | 15.339 | 868.940 | 85.088 | 0.9652 | −0.30 | SL |
| 300.010 | 16.750 | 881.293 | 87.887 | 0.9937 | −0.31 | SL |
| 300.010 | 17.818 | 889.811 | 90.070 | 1.0193 | −0.11 | SL |
| 323.150 | 1.943 | 34.497 | 16.297 | 0.1560 | −0.55 | SG |
| 323.150 | 2.972 | 55.423 | 16.552 | 0.1677 | −0.44 | SG |
| 323.150 | 3.977 | 78.294 | 16.948 | 0.1764 | 0.03 | SG |
| 323.150 | 5.233 | 111.469 | 17.554 | 0.1862 | 0.27 | SG |
| 323.150 | 7.999 | 219.115 | 20.530 | 0.2223 | 1.21 | SC |
| 323.150 | 10.094 | 395.603 | 28.556 | 0.3549 | 0.32 | SC |
| 323.150 | 12.410 | 608.353 | 45.929 | 0.5188 | 0.10 | SC |
| 323.151 | 14.819 | 695.203 | 56.502 | 0.6296 | 0.60 | SC |
| 323.150 | 18.435 | 763.559 | 66.228 | 0.7366 | 0.25 | SC |
| 348.140 | 3.824 | 66.037 | 18.038 | 0.1802 | 0.15 | SG |
| 348.141 | 4.942 | 89.195 | 18.442 | 0.1880 | 0.34 | SG |
| 348.140 | 6.236 | 119.051 | 19.207 | 0.1987 | 1.40 | SG |
| 348.150 | 9.697 | 222.203 | 22.129 | 0.2333 | 1.94 | SC |
| 348.150 | 12.499 | 342.029 | 27.124 | 0.2908 | 1.38 | SC |
| 348.148 | 14.749 | 451.854 | 33.842 | 0.3661 | 1.28 | SC |
| 348.151 | 17.778 | 568.163 | 42.848 | 0.6526 | −0.32 | SC |
| 348.149 | 19.233 | 608.215 | 46.356 | 0.5027 | −1.35 | SC |

[a] SL: Subcooled Liquid; SG: Superheated Gas; SC: Supercritical.

Berger *et al* [33] are plotted together with the data from Van der Gulik [38] at 280 K, in figure 5. Despite of small, reported uncertainty of ±0.5% by Padua *et al* [39], unusual damping using the vibrating-wire was reported by [38], and a large offset is seen in figure 5. For the isotherm at 298 K, the data of this work correspond well with the data of Iwasaki and Takahashi [37], which is the most extensive study of the viscosity in the critical region. For the isotherm at 300 K, the deviation from Kestin *et al* [36] and Van Der Gulik [38] is due to the operating temperature of 304 K in their work, fairly close to the critical temperature of CO2 and 4 K higher than the operating temperature in this work.

The data shown for 298.15 K depicts both gas and liquid phases, where the phase shift occurs at 6.4 MPa. There is a good consistency between the measurements in both gas and liquid phases. The performance of the viscometer at relatively lower pressures were checked by comparison with the reliable data recently published by Humberg [9] with the relative uncertainty of 0.5%. The plots at 298.15 K and 323.15 K show the $CO_2$ is in the superheated gas phase for pressures below 6.4 MPa and 7.3 MPa, respectively. The observed maximum deviation between the data from this work and data from Humberg [9] is 0.57%, which is comparable with the uncertainty of the data.

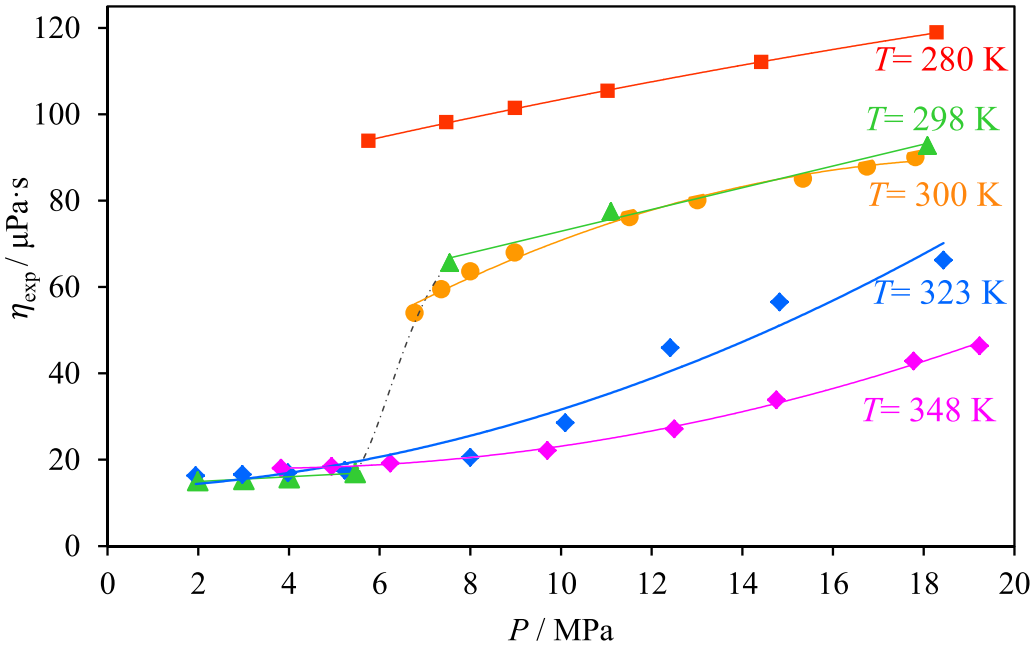


**Figure 4.** Viscosity data for pure $CO_2$ are plotted versus pressure. The markers present the measured viscosity $\eta_{exp}$. The lines correspond to the polynomial fit to the experimental data. The dashed line shows phase change at 298 K.

**Table 6.** List of data sources for the viscosity of pure $CO_2$ used.

| Source | Temperature range/K | Pressure range/MPa | Reported uncertainty | Phase[a] | Method |
|---|---|---|---|---|---|
| Golubev and Petrov [34] | 293.15–523.15 | 0.1–80 | — | L | Capillary flow |
| Michels *et al* [35] | 273.15–348.15 | 0.9–209.7 | — | G & L | Capillary flow |
| Kestin *et al* [36] | 297–525 | 0.126–6.85 | 0.5% | G & L | Oscillating disk |
| Kestin *et al* [36] | 298.3–323.3 | 3.7–11.9 | | | Oscillating disk |
| Iwasaki and Takahashi [37] | 298.15–323.15 | 0.1–14.5 | 0.3% | G & L | oscillating disk viscometer |
| Van der Gulik [38] | 220.01–308.15 | 0.56–453.20 | 1% | L | Vibrating wire |
| P´adua *et al* [39] | 260, 280, and 300 | 5.95–100 | ±0.5% | L | Vibrating wire |
| Pensado *et al* [40] | 303.15–353.15 | 10–60 | 3% | G & L | Vibrating wire |
| Nazeri *et al* [7] | 238.2–423.2 | 0.1–150 | ±2% | | Capillary viscometer |
| Humberg *et al* [9] | 253.15–473.15 | 0.1–14 | 0.34%–0.48% | | Rotating body |

[a] G: Gas phase; L: Liquid phase.

The measured viscosity of $CO_2$ at 343 K deviates significantly from the model predictions, with a maximum deviation of 2%. Instead, there is a close agreement between measured data of this work with the data from Hendl *et al* [29], with the maximum deviation of 1.15%. Hendl *et al* [29] has not estimated the uncertainty of the viscosity data and observed an abnormal behaviour in the critical region. The reason for significant deviations at 343 K requires further investigations as all reported data have been performed using the same apparatus type, a capillary viscometer. There is only one more secondary data set at this temperature in the literature by Pensado *et al* [40] who measured the viscosity of $CO_2$ with a vibrating-wire viscometer with a high uncertainty of 3%. Nevertheless, only two data points were found to match with the pressures up to 20 MPa. Note that the uncertainty of the reference correlation [13] within the operating conditions in this work is between 1%, 2%–3% and 4% for the gas, supercritical and liquid phases, as illustrated in figure 25, in the [13].

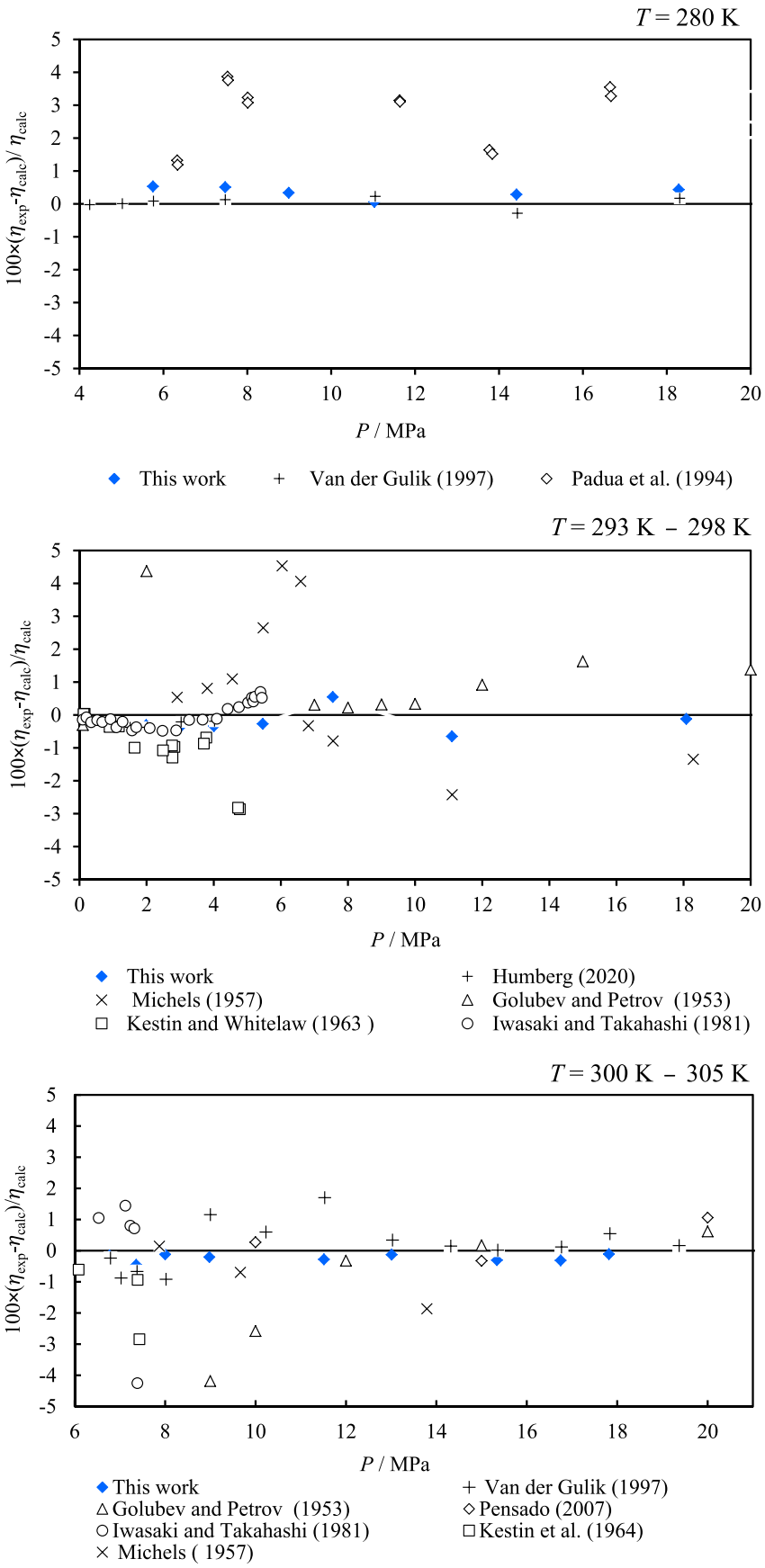


**Figure 5.** Relative deviations between experimental and calculated viscosity values, $\eta_{exp}$ and $\eta_{calc}$, for pure $CO_2$. $\eta_{calc}$ is the reference correlation [13] implemented in NIST REFPROP 10.0 database [14]. Deviations are plotted versus pressure at different temperature ranges.

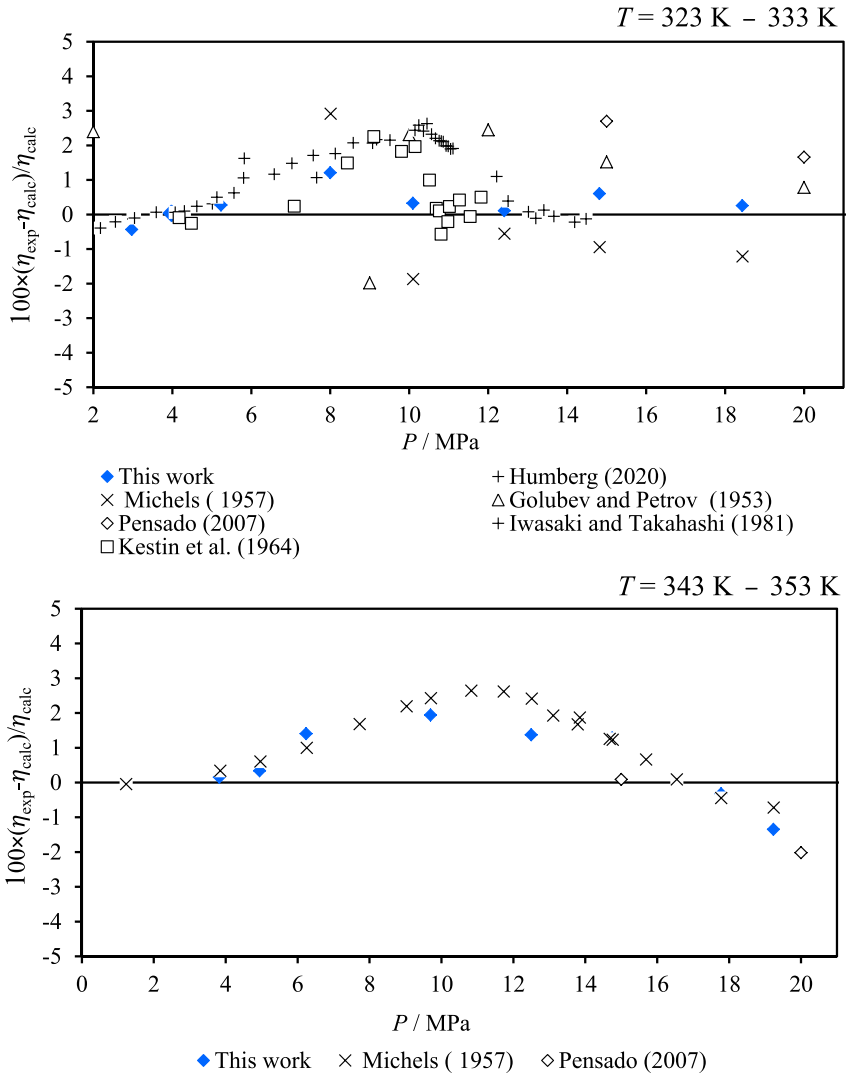


**Figure 5.** (Continued.)

## 7. Conclusions

Viscosity measurements were carried out for pure $CO_2$ at five isotherms and pressures between 2 MPa and 20 MPa using a new two-capillary viscometer to validate the performance of the viscometer and the new measurements approach A modified hydrodynamic model for high pressure and liquid $CO_2$ has been described. The modified hydrodynamic model was used to calculate dynamic viscosities for $CO_2$. The obtained viscosities are in agreement with the model predictions and are within the estimated uncertainty of the data. Experimental deviation from model predictions were observed at 343–353 K for $CO_2$, suggesting further investigations are required. The uncertainty analysis shows a maximum extended combined uncertainty of 1.3% within all thermodynamic states of gas, liquid, and close to the critical region.

Several suggestions were provided for potential improvements in the viscosity measurement to enhance the accuracy of the data for further worked, including using different capillary configuration. An optimum capillary configuration results in operating the viscometer at higher flow rates, consequently, to reduce the uncertainty arising from low pressure drop. Another suggestion is to use a different reference fluid than helium. Calibrating mass flow rates with helium as the reference fluid led to higher measurement uncertainty due to the low molecular weight. To improve, using a reference gas with higher molecular weight and known reference viscosity like $N_2$ or Ar could be better alternatives. The potential leakage at high pressures was another source of uncertainties. In addition, the correction parameters used in this study were from the existing literature. However, more research is needed to understand the impact of different correction factors, especially at high pressures and in liquid phases. For example, viscosity measurements at low pressures are needed to determine the virial viscosity coefficient, particularly for helium. By implementing these suggestions, it may be possible to achieve even greater accuracy in future measurements, allowing for improved measurements of $CO_2$ and $CO_2$–rich mixtures where experimental data are most lacking.

## Acknowledgments

This publication has been produced with support from the from the research program CLIMIT and the NCCS Centre, performed under the Norwegian research program Centers for Environment-friendly Energy Research (FME). The authors acknowledge the following partners for their contributions: Aker Solutions, ANSALDO Energia, CoorsTek Membrane Sciences, EMGS, Equinor, Gassco, KROHNE, Larvik Shipping, Lundin, Norcem, Norwegian Oil and Gas, Quad Geometrics, TOTAL, and the Research Council of Norway (257579/E20 and 280394).

## Appendix A. Stress on the capillary walls

For tube or cylinder with inner radius $r_\mathrm{i}$ and outer radius $r_\mathrm{o}$ is subjected to internal and external pressure, $P_\mathrm{i}$ and $P_\mathrm{o}$, respectively, three different stresses are explained below [42]. Stress in axial direction at a point in the tube or cylinder wall can be expressed as:

$$\tau_a = \frac{P_\mathrm{i} r_\mathrm{i}^2 - P_\mathrm{o} r_\mathrm{o}^2}{r_\mathrm{o}^2 - r_\mathrm{i}^2}. \tag{A-1}$$

Stress in circumferential direction—Hoop Stress at a point in the tube or cylinder wall can be expressed as:

$$\tau_c = \frac{P_\mathrm{i} r_\mathrm{i}^2 - P_\mathrm{o} r_\mathrm{o}^2}{r_\mathrm{o}^2 - r_\mathrm{i}^2} - \frac{r_\mathrm{i}^2 r_\mathrm{o}^2 \left(P_\mathrm{o} - P_\mathrm{i}\right)}{r^2 \left(r_\mathrm{o}^2 - r_\mathrm{i}^2\right)} \tag{A-2}$$

where $r$ is the radius to point in tube or cylinder wall ($r_\mathrm{i} < r < r_\mathrm{o}$) and maximum stress occurs when $r = r_\mathrm{i}$.

Stress in radial direction when $r$ is the maximum stress occurs when $r = r_\mathrm{o}$ is defined as:

$$\tau_r = \frac{P_\mathrm{i} r_\mathrm{i}^2 - P_\mathrm{o} r_\mathrm{o}^2}{r_\mathrm{o}^2 - r_\mathrm{i}^2} + \frac{r_\mathrm{i}^2 r_\mathrm{o}^2 \left(P_\mathrm{o} - P_\mathrm{i}\right)}{r^2 \left(r_\mathrm{o}^2 - r_\mathrm{i}^2\right)} \tag{A-3}$$

## Appendix B. Uncertainty in temperature from ITS-90 calibrations

**Table B.1.** The uncertainty of fixed-point cells (by coverage factor $k = 2$, providing a level of confidence of approximately 95%).

| Fixed point cell | Uncertainty/mK |
|---|---|
| Triple point of mercury (T90 ≡ 234.3156 K) | ± 1 |
| Triple point of water (T90 ≡ 273.16 K) | ± 0.1 |
| Melting point of gallium (T90 ≡ 302.9146 K) | ± 1.2 |
| Freezing point of indium (T90 ≡ 429.7485 K) | ± 2 |

## Appendix C. Uncertainty in pressure

**Table C.1.** The uncertainty of piston cells used for the pressure calibration.

| Piston cell | Uncertainty |
|---|---|
| up to 1 MPa | 0.000 02 MPa + 0.01% RDG[a] |
| 1–5 MPa | 0.0001 MPa + 0.01% RDG |
| 5–20 MPa | 0.0004 MPa + 0.01% RDG |

[a] Reading.

**Table C.2.** The combined uncertainty of pressure sensors from pressure calibration.

| | Model and pressure range | Pressure sensors | $U_c$ ($P$)/kPa |
|---|---|---|---|
| Inlet of upstream capillaries | Keller 100 MPa | PS11 | 5.726 |
| | Paroscientific Digiquarts 13.8 MPa | PS14 | 2.285 |
| | Paroscientific Digiquarts 6.9 MPa | PS13 | 0.434 |
| | Paroscientific Digiquartz 2.1 MPa | PS15 | 0.251 |
| Outlet of upstream capillaries | Keller 100 MPa | PS21 | 1.983 |
| | Paroscientific Digiquarts 13.8 MPa | PS24 | 1.094 |
| | Paroscientific Digiquarts 6.9 MPa | PS23 | 0.264 |
| | Paroscientific Digiquartz 2.1 MPa | PS25 | 0.0612 |
| Inlet of downstream capillaries | Paroscientific Digiquartz 6.9 MPa | PS31 | 0.012 |
| | Paroscientific Digiquartz 0.21 MPa | PS32 | 0.007 |
| Outlet of downstream capillaries | Paroscientific Digiquartz 6.9 MPa | PS41 | 0.006 |
| | Paroscientific Digiquartz 6.9 MPa | PS42 | 0.008 |

## Appendix D. Uncertainty in pressure drop

For each data point, the measure pressure $P_M$ using a pressure sensor is equal to:

$$\boldsymbol{P_M} = \boldsymbol{P} + \boldsymbol{e_r} + \boldsymbol{e_s}(\boldsymbol{P}) \tag{D-1}$$

where $P$ is the actual value of pressure, $e_r$ is the random error of measurement and $e_s(P)$ is referred to the systematic error which is a function of pressure. The $e_s(P)$ is here only function of pressure and determined through the pressure calibration (from the factors that they do not change during one experiment). The bias measurements before and after each measurement need to be performed for accurate pressure drop measurements. The pressure drop along capillary with $P_{in}$ and $P_{out}$ at inlet and outlet one can write:

$$\Delta P_M = (P_{in,\,M} - P_{in,MB}) - (P_{out,M} - P_{out,\,MB}) \tag{D-2}$$

where $P_M$ and $P_{MB}$ are the measured and bias measurements, respectively. The pressure values are given by:

$$\begin{aligned} P_{in,\,M} &= P_{in} + e_{in,r} + e_{in,s}(P_{in}) \\ P_{in,\,MB} &= P_{in,B} + e_{in,r,\,B} + e_{in,s}(P_{in,B}) \\ P_{in,\,MB} &= P_{in,B} + e_{in,r,\,B} + e_{in,s}(P_{in,B}) \\ P_{out,\,MB} &= P_{out,B} + e_{out,r,\,B} + e_{out,s}(P_{out,B}) \end{aligned} . \tag{D-3}$$

Here $P_B$ is the bias pressure By combining equations (D-2) and (D-3):

$$\begin{aligned} \Delta P_M = {} & (P_{in} - P_{out}) - (P_{in,\,B} - P_{out,\,B}) + (e_{in,r} - e_{out,r}) \\ & - (e_{in,r,B} - e_{out,r,B}) + (e_{in,s}(P_{in}) - e_{out,s}(P_{out})) \\ & - (e_{in,s}(P_{in,B}) - e_{out,s}(P_{out,B})). \end{aligned} \tag{D-4}$$

It is assumed that $P_{in,MB} = P_{out,MB} = P_B$, although they are usually different because of the measurement error. The random error can be added to one term:

$$e_r = (e_{in,r} - e_{out,r}) - (e_{in,r,B} - e_{out,r,B}). \tag{D-5}$$

And the systematic error can be derived from:

$$e_{in,s}(P_{in}) - e_{in,s}(P_B) \approx \frac{\partial e_{in,s}}{\partial P}(P_{in} - P_B) \tag{D-6}$$

$$e_{out,s}(P_{out}) - e_{out,s}(P_B) \approx \frac{\partial e_{out,s}}{\partial P}(P_{out} - P_B) \tag{D-7}$$

$$\Delta P_M = \Delta P + e_r + \frac{\partial e_{in,s}}{\partial P}(P_{in} - P_B) + \frac{\partial e_{out,s}}{\partial P}(P_{out} - P_B). \tag{D-8}$$

The uncertainty of each term is introduced as:

$$u_{in,B} = u\left(\frac{\partial e_{in,s}}{\partial P}\right),\ u_{out,B} = u\left(\frac{\partial e_{out,s}}{\partial P}\right), \tag{D-9}$$

If we assume each term is independent, it gives:

$$u^2(\Delta P_M) = u^2(e_r) + (P_{in} - P_B)^2 u_{in,B}^2 + (P_{out} - P_B)^2 u_{out,B}^2. \tag{D-10}$$

However, if the term $e_{in,s}$ and $e_{out,s}$ are not independent, then their terms need to be summed and one get:

$$u^2(\Delta P_M) = u^2(e_r) + ((P_{in} - P_B)u_{in,B} + (P_{out} - P_B)u_{out,B})^2. \tag{D-11}$$

By assuming $u_{in,B}$ and $u_{out,B}$ are equal $u_{in,B} = u_{out,B} = u_B$, the total uncertainty becomes:

$$u^2(\Delta P_M) = u^2(e_r) + \Delta P^2 u_B^2. \tag{D-12}$$

Here $u_r$ can be found from the repeatability of the measurement. One assumption to determine $u_B$ is that $e_s(0) = 0$ and the maximum uncertainty of pressure sensor at the pressure of $P_{max}$ is $u(P_{max})$. Hence for any pressure $P$ over the range of pressure sensor with a linear assumption, one can write:

$$u_B = \frac{u(P_{max})}{P_{max}} \tag{D-13}$$

## ORCID iD

Anders Austegard https://orcid.org/0000-0001-9252-4618

## References


[1] Li H, Wilhelmsen Ø and Yan J 2015 Properties of $CO_2$ mixtures and impacts on carbon capture and storage *Handbook Clean Energy Systems* (Wiley) pp 1–17

[2] Wetenhall B *et al* 2014 Impact of $CO_2$ impurity on $CO_2$ compression, liquefaction and transportation *Energy Proc.* **63** 2764–78

[3] Li H, Wilhelmsen Ø, Lv Y, Wang W and Yan J 2011 Viscosities, thermal conductivities and diffusion coefficients of $CO_2$ mixtures: review of experimental data and theoretical models *Int. J. Greenhouse Gas Control* **5** 1119–39

[4] Løvseth S W, Stang H G J, Austegard A, Westman S F, Span R and Wegge R 2016 Measurements of $CO_2$-rich mixture properties: status and CCS needs *Energy Proc.* **86** 469–78

[5] Munkejord S T, Hammer M and Løvseth S W 2016 $CO_2$ transport: data and models–A review *Appl. Energy* **169** 499–523

[6] Al-Siyabi I 2013 *Effect of Impurities on $CO_2$ Stream Properties* (Heriot-Watt University)

[7] Nazeri M, Chapoy A, Burgass R and Tohidi B 2018 Viscosity of $CO_2$-rich mixtures from 243 K to 423 K at pressures up to 155 MPa: new experimental viscosity data and modelling *J. Chem. Thermodyn.* **118** 100–14

[8] Khosravi B, Betken B, Jakobsen J P, Løvseth S W and Span R 2022 Viscosity measurements of $CO_2$-rich; $CO_2 + N_2$ and $CO_2 + H_2$ mixtures in gas or supercritical phase at temperatures between 273 and 473 K and pressures up to 8.7 MPa *Fluid Phase Equilib.* **560** 113519

[9] Humberg K 2020 Viscosity measurements of binary gas mixtures and analysis of approaches for the modeling of mixture viscosities *Dissertation* Ruhr-Universität Bochum, Bochum

[10] Khosravi B, Austegard A, Lovseth S W, Stang H J and Jakobsen J P 2024 A two-capillary viscometer for temperatures up to 473 K and pressures up to 100 MPa—operation and verification at low pressure *Metrologia* **61** 035008

[11] May E F *et al* 2006 Transport properties of argon at zero density from viscosity-ratio measurements *Metrologia* **43** 247

[12] Berg R F, May E F and Moldover M R 2014 Viscosity ratio measurements with capillary viscometers *J. Chem. Eng. Data* **59** 116–24

[13] Laesecke A and Muzny C D 2017 Reference correlation for the viscosity of carbon dioxide *J. Phys. Chem. Ref. Data* **46** 013107

[14] Lemmon E W *et al* 2018 *NIST Standard Reference Database 23: Reference Fluid Thermodynamic and Transport properties-REFPROP, Version 10.0, National Institute of Standards and Technology* (Standard Reference Data Program)

[15] Poiseuille J L M 1844 *Recherches expérimentales sur le mouvement des liquides dans les tubes de très-petits diamètres* vol 11 (Imprimerie Royale) pp 961–7

[16] Berg R F 2004 Quartz capillary flow meter for gases *Rev. Sci. Instrum.* **75** 772–9

[17] Cencek W, Przybytek M, Komasa J, Mehl J B, Jeziorski B and Szalewicz K 2012 Effects of adiabatic, relativistic, and quantum electrodynamics interactions on the pair potential and thermophysical properties of helium *J. Chem. Phys.* **136** 224303

[18] Jcgm J 2008 Evaluation of measurement data—Guide to the expression of uncertainty in measurement *Int. Organ. Stand. Geneva* **50** 134

[19] Mangum B 1989 The new international temperature scale of 1990 (ITS-90) *Clin. Chem.* **35** 503–5

[20] Mason E and Kronstadt B 1967 Graham's laws of diffusion and effusion *J. Chem. Educ.* **44** 740

[21] Berg R F and Moldover M R 2012 Recommended viscosities of 11 dilute gases at 25 C *J. Phys. Chem. Ref. Data* **41** 043104

[22] Span R and Wagner W 1996 A new equation of state for carbon dioxide covering the fluid region from the triple-point temperature to 1100 K at pressures up to 800 MPa *J. Phys. Chem. Ref. Data* **25** 1509–96

[23] Ortiz-Vega D *et al* 2020 Helmholtz equation of state for helium *J. Phys. Chem. Ref. Data* (https://doi.org/10.6028/NIST.IR.8474)

[24] Huber M L, Sykioti E A, Assael M J and Perkins R A 2016 Reference correlation of the thermal conductivity of carbon dioxide from the triple point to 1100 K and up to 200 MPa *J. Phys. Chem. Ref. Data* **45** 013102

[25] Hands B and Arp V 1981 A correlation of thermal conductivity data for helium *Cryogenics* **21** 697–703

[26] Kawata M *et al* 1991 Capillary viscometers. Measurement of the transport properties of fluids *Measurement of the Transport Properties of Fluids* (Blackwell) pp 49–75

[27] Schäfer M 2016 Improvements to two viscometers based on a magnetic suspension coupling and measurements on carbon dioxide *Doctoral Dissertation* Ruhr-Universität Bochum, Bochum

[28] Vogel E 2016 The viscosities of dilute Kr, Xe, and CO _2 2 revisited: new experimental reference data at temperatures from 295 K to 690 K *Int. J. Thermophys.* **37** 1–20

[29] Hendl S, Neumann A-K and Vogel E 1993 The viscosity of carbon dioxide and its initial density dependence *ECTP: European Conf. on Thermophysical Properties* (*Lisboa*, *30 August 1993*) vol 25 pp 503–11

[30] Gracki J, Flynn G and Ross J 1969 Viscosity of Nitrogen, Helium, Hydrogen, and Argon from− 100 to 25 c up to 150–250 atm *J. Chem. Phys.* **51** 3856–63

[31] Sharipov F 2003 Application of the Cercignani–Lampis scattering kernel to calculations of rarefied gas flows. II. Slip and jump coefficients *Eur. J. Mech.* B **22** 133–43

[32] Kawata M 1974 Laminar flow and pressure drop in capillary tube

[33] Berger S, Talbot A L and Yao L 1983 Flow in curved pipes *Annu. Rev. Fluid Mech.* **15** 461–512

[34] Golubev I and Petrov V 1953 Trudy Gos. Nauchno-is sled. proektn, in-ta azotn, prom-sti vol 2 p p5

[35] Michels A, Botzen A and Schuurman W 1957 The viscosity of carbon dioxide between 0 C and 75 C and at pressures up to 2000 atmospheres *Physica* **23** 95–102

[36] Kestin J, Whitelaw J H and Zien T 1964 The viscocity of carbon dioxide in the neighbourhood of the critical point *Physica* **30** 161–81

[37] Iwasaki H and Takahashi M 1981 Viscosity of carbon dioxide and ethane *J. Chem. Phys.* **74** 1930–43

[38] Van Der Gulik P 1997 Viscosity of carbon dioxide in the liquid phase *Physica* A **238** 81–112

[39] Padua A, Wakeham W and Wilhelm J 1994 The viscosity of liquid carbon dioxide *Int. J. Thermophys.* **15** 767–77
[40] Pensado A S, Pádua A A H, Comuñas M J P and Fernández J 2008 Viscosity and density measurements for carbon dioxide+ pentaerythritol ester lubricant mixtures at low lubricant concentration *J. Supercrit. Fluids* **44** 172–85
[41] Vesovic V, Wakeham W A, Olchowy G A, Sengers J V, Watson J T R and Millat J 1990 The transport properties of carbon dioxide *J. Phys. Chem. Ref. Data* **19** 763–808
[42] Engineering ToolBox 2005 Stress in thick-walled cylinders or tubes (available at: www.engineeringtoolbox.com/stress-thick-walled-tube-d_949.html)